RESEARCH ARTICLE

Metamaterial Absorber Structure for Tx-Rx Antenna Isolation Improvement in Full-Duplex Massive MIMO

YUANZHE GONG, (Graduate Student Member, IEEE), **ROBERT MORAWSKI**, **AND THO LE-NGOC**, (Life Fellow, IEEE)

Department of Electrical and Computer Engineering, McGill University, Montreal, QC H3A 0E9, Canada

Corresponding author: Yuanzhe Gong (yuanzhe.gong@mail.mcgill.ca)

ABSTRACT This paper presents a novel metamaterial absorber structure for Tx-Rx antenna isolation improvement in the in-band full-duplex massive MIMO systems. The design processes of the absorber unit element, structure and placement, and their impacts on the beamforming radiation patterns are studied. The illustrative result indicates an over 99.8% power absorption at 3.49 GHz. Working with our 8×8Tx/8×8Rx full-duplex antenna array prototype, an average Tx-Rx antenna element mutual coupling level of -65.4 dB can be achieved between the closest Tx-Rx element pairs, indicating an improvement of 17.5 dB isolation by adding the absorber. The absorber structure's effectiveness in suppressing beam-level self-interference is studied. The experimental measurement results, utilizing sample Tx/Rx 1×8 antenna sub-arrays, show an average beam-level isolation enhancement of 18.6 dB in near-field coupling dominant scenarios. Integrated with a simple angular perturbation beam isolation technique, an average Tx-Rx beam-level isolation of 90.8 dB and a maximum beam isolation of 104.4 dB can be reached in the Tx/Rx beam steering range $-48°$ to $48°$ with 20 MHz modulated signals. The experiment illustrates the metamaterial absorber structure has a negligible influence on the far-field beam pattern in the beamforming process. Simulation and measured results on beam radiation patterns and far-field and near-field isolation improvement in different scenarios are investigated and shown to be in good agreement.

INDEX TERMS Metamaterial absorber, full-duplex, massive MIMO, mutual coupling, beam patterns, beamforming, isolation.

I. INTRODUCTION

Driving the quest for systems to reach higher spectral efficiency, full-duplex (FD) operation has gained an increasing amount of attention in wireless communication research [1], [2], [3]. FD communications, with their capability to simultaneously send and receive signals in the same frequency band, can theoretically double spectral efficiency with a reduced latency. However, a major challenge hindering widespread FD deployment is the issue of high-power self-interference (SI), which is the interference that an FD terminal causes

to itself while transmitting to prevent that terminal from receiving the desired signal. The SI can significantly degrade the signal-to-interference-and-noise ratio (SINR) and the system throughput.

To preserve FD performance, employing a combination of Tx-Rx isolation and SI cancellation (SIC) techniques is crucial [1], [4], [5], [6]. These techniques aim to reduce residual SI to a level comparable to the thermal noise, thus preventing substantial degradation of SINR. Isolation techniques primarily focus on diminishing parasitic signal propagation from the transmitter (Tx) to its receiver (Rx), thereby effectively suppressing the intensity of mutual coupling (MC) waves at the receiver. The residual SI is then

The associate editor coordinating the review of this manuscript and approving it for publication was Ravi Kumar Gangwar.

further mitigated through SIC, which involves subtracting the interference in the receiver's path using a modified copy of the transmitted signal. However, due to practical limitations, such as nonlinearities in the Tx amplifiers and the constrained dynamic range of the Rx analog-to-digital converter (ADC), isolation techniques are necessary to serve as the first line of defence against SI. It not only simplifies the baseband precoding but also helps to prevent the saturation of the ADC in scenarios with excessive SI. As illustrated in [5], achieving a minimum of 40 dB isolation is necessary even in low-end, relaxed FD scenarios. In more demanding, high-end scenarios, an isolation ranging from 60 dB to 80 dB is essential for maintaining the integrity of FD systems.

A. RELATED WORKS

In the isolation design, one common strategy is increasing the separation distance between local Tx and Rx antennas, resulting in a higher path loss [4], [7], [8], [9]. However, the approach often encounters limitations in system compactness, which hampers its practical use in space-constrained environments. Another effective isolation improvement strategy involves optimizing the cross-polarization between the Tx and Rx antennas, which can effectively diminish the intensity of coupling waves received by the Rx antenna. Experiments have shown that more than 10 dB additional isolation can be achieved [5], [8], [10], [11]. However, it is important to note that the effectiveness of the beamforming process depends on the polarization purity performance, which may vary at different beam steering angles due to the dynamic nature of beamforming in practical scenarios. A variety of decoupling and frequency selective surface (FSS) structures have been explored to reduce or eliminate wave coupling [12]. For instance, in [13], a π-shaped decoupling structure was implemented, demonstrating more than 24 dB of co-polarization isolation improvement and an achievable total isolation of 37 dB in the experiment with 1×2 MIMO arrays. Similarly, [14] introduced a diamond-shaped decoupling network comprising two symmetrical L-shaped inverted-F antennas to a two-port MIMO antenna, achieving an MC mitigation level of 16 dB. In [15], a combination of metallic wall barriers and metallic pins is strategically used to create a short between the patch and the ground. This design effectively reduces surface wave and free space coupling in the sub-6 GHz region, leading to a 19 dB and 15 dB reduction in E- and H-plane couplings, respectively. A novel decoupling structure employing a parasitic element to emit orthogonally polarized fields is introduced in [16], effectively nullifying the original coupling field around the Rx antenna in a collinear FD dipole array, bringing the total isolation to 50 dB. Similarly, in [17], the isolation in FD dielectric resonator antennas (DRAs) system is enhanced through the orthogonal arrangement of two identical linearly polarized resonators. A lossless network decoupling technique is employed in [18], utilizing antenna scattering matrix representation and spherical vector wave

expansion, specifically targeting narrowband FD systems. Other isolation improvement approaches including out-of-phase near-field cancellation coupling circuits [16], [19], [20], defected ground structure (DGS) [21], [22], and electromagnetic band-gap (EBG) structures [23], [24] have demonstrated impressive effectiveness in MC mitigation and an over 40 dB total isolation can be achieved combined with techniques of antenna separation and cross-polarization design. However, the practical application of these strategies [5], [10], [11], [13], [14], [15], [16], [17], [18], [19], [20], [21], [22], [23], [24] is generally confined to systems with a limited number of antenna elements. This limitation arises because incorporating additional structures can lead to excessive complexity in large-scale antenna array designs and can potentially impact the radiation patterns due to the adjustment of the structure's electromagnetic (EM) characteristics and the introduction of extra reflections. While the isolation enhancement techniques reviewed in [12] address MC mitigation in massive Multiple-Input Multiple-Output (mMIMO) systems, the research primarily concentrates on half-duplex (HD) scenarios, where inter-element MC within the array is the primary concern. Meanwhile, the impact of adding structures on array beamforming performance requires further investigation.

Without requiring any modifications to the original antenna configuration, the absorber is one of the promising technologies to improve the Tx-Rx isolation in the FD systems. As shown in [9], using radio frequency (RF) absorbers alongside directional antennas and strategic spacing can achieve a maximum total Tx-Rx isolation level of 73.8 dB, indicating more than 10 dB isolation improvement via blocking and absorbing the line-of-sight (LoS) coupling waves. However, there is usually a tradeoff between the thickness and the height of the conventional RF absorber and the effectiveness of the absorption. First proposed in [25], metamaterial absorbers have gained more and more popularity due to their advantages of adjustable effective permittivity and permeability, low profile, easy fabrication, and low reflectivity. A typical metamaterial is seen to have elements with sizes smaller than $0.2\lambda_0 \times 0.2\lambda_0$ and a thickness less than $0.04\lambda_0$, where λ_0 represents the free-space wavelength [26], [27], [28], [29]. Consequently, the metamaterial absorber is more adaptable and flexible due to its small and adjustable size, allowing it to be inserted in various antenna systems without altering the size of the entire system. The metamaterial absorber structures typically consist of periodic top metallic patch circuits and ground metal planes separated by dielectric substrates. Therefore, the fabrication can take advantage of the PCB manufacturing process. Interaction between the homogenized structures creates the electric and magnetic response. The separation between the top conductor circuit and the ground plane can achieve an electric Drude response from the ground plane plus a Drude-Lorentz response from the top metallic circuit [30]. The magnetic response transfers the incident coupling waves to the surface current on the top-layer

TABLE 1. Comparison of absorber structures in the literature.

Ref.	Half-/Full-Duplex	Operating Frequency	Absorber Type	Mounted position	Absorber Element Size (λ_0) (length × width× thickness)	Absorber Isolation Improvement	Total Isolation Level
[9]	FD	2.45 GHz	Conventional ABS	Vertical		10.1 dB	73.8 dB
[29]	HD	2.4 GHz	Metamaterial	Vertical	0.17×0.16×0.013	16 dB	42 dB
[31]	HD	3.4 GHz	Metamaterial	Horizontal	0.12×0.25	27 dB	52 dB
[32]	HD	5.1 GHz	Metamaterial	Horizontal	0.08×0.06	10 dB	29 dB
[33]	HD	5.1 GHz	Metamaterial	Horizontal	0.20×0.20	10.5 dB	33 dB
[28]	FD	1.27 GHz	Metamaterial	Vertical	0.19×0.19×0.03	8 dB	22 dB
This work	FD	3.5 GHz	Metamaterial	Vertical	0.19×0.19×0.04	18.6 dB (avg) 42.0 dB (best)	90.8 dB (avg) 104.4 dB (best)

metallic circuit. Adjusting the geometry of the metallic circuits and the spacing of the two metallic structures changes the resonant frequency position and strength of a Lorentz resonance and modifies the magnetic response. When the effective permittivity ($\widetilde{\epsilon}$) and effective permeability ($\widetilde{\mu}$) of the homogenized structure are adjusted to be equal to each other, i.e., $\widetilde{\epsilon}/\widetilde{\mu} = 1$, the structure's input impedance closely matches the impedance of the air, and low reflection at the intersections of the air and the absorber surface can be realized. A significant amount of coupling wave can go into the absorber structure and dissipate in the dielectric substrate. Illustrative results show a power absorption rate over 90% [26], [27], [28] and an isolation improvement more than 10 dB [29], [31], [32], [33], [34]. In [28], a double-layer metamaterial absorber is employed in a four-element FD antenna array. Experimental findings indicate the absorber contributes to an SI suppression around 8 dB, resulting in a total isolation of 22 dB. The study in [35] demonstrates a reduction of MC by 8 dB between sub-arrays in a large 3 × 8 array MIMO, achieved through the orthogonal placement of a metamaterial absorber between neighbouring sub-arrays. Table 1 summarizes and compares recent absorber research and the achieved isolation improvement.

Nonetheless, it is noticeable that only a few publications specifically address the metamaterial absorber structure in FD scenarios. In addition, most existing research on metamaterial absorbers for isolation improvement focuses on systems with a limited number of antenna elements. For example, studies [9], [26], [27], [28], [29], [31], [32], and [33] explore antenna systems comprising no more than four elements. While [35] utilizes the metamaterial absorber for a 3 × 8 array, further investigation is needed to understand the absorber's impact on beam patterns and how beamforming affects the absorber's effectiveness. Given the substantial potential of large-scale antenna arrays to enhance isolation through directional and controllable beams, their application in FD designs is crucial. As demonstrated in [36], antenna arrays effectively suppress SI by steering beams toward the radiation nulls of interference sources. Combined with antenna isolation techniques, an average beam-level isolation of 65.6 dB can be reached. Despite the efficacy of controlling far-field beam directions in reducing SI, the persistent challenge posed by near-field coupling components remains a crucial factor limiting the overall

isolation performance. In this context, metamaterials can emerge as a promising solution to address these near-field coupling issues. Therefore, the integration of metamaterial absorbers with large-scale FD antenna arrays has the potential to significantly enhance the total isolation performance. Despite the potential benefits, there is a noticeable gap in experimental research demonstrating the effectiveness of metamaterials in mitigating near-field SI and their subsequent impacts on the far-field beamforming in FD mMIMO systems.

Additionally, to leverage the isolation benefits of beamforming in large-scale arrays without incurring excessive complexity, the hybrid precoding/combining (HPC) technique emerges as a pivotal approach in FD mMIMO systems. Research presented in [37] has developed an HPC scheme that minimizes SI by controlling the angles-of-departure and angles-of-arrival of the Tx and Rx antenna arrays, leading to an 81.5 dB and 44.5 dB SI suppression in the far-field and near-field components, respectively. Then, an HPC approach for the Multi-User (MU) mMIMO system is proposed in [38]. This strategy enables simultaneous service to multiple users, suppression of the SI channel, and maximization of the sum-rate capacity, achieving a remarkable total SI suppression level of 78.1 dB in FD mMIMO. Furthermore, [39] introduces an HPC implementation that employs a zero-space SIC method, leveraging correlated mmWave channel characteristics, specifically for full-duplex amplify-and-forward mmWave relay systems.

However, the evaluation of SI suppression performance in current studies [37], [38], [39] often relies heavily on theoretical models, including line-of-sight (LoS) near-field and reflected non-line-of-sight (NLoS) SI channel models, through simulation results. The dynamic nature of antenna array radiation, which is influenced by factors such as inter-element MC and variations in feeding signals, suggests that these models might not fully capture the practical complexities of the SI channel. Therefore, there is a pressing need for experimental studies to assess the actual level of SI suppression achievable in real-world conditions. Furthermore, there is a notable lack of experimental research exploring the correlations between the Tx/Rx beam directions and the variations of isolation performance. Investigating this relationship experimentally could yield critical insights into the interactions among various SI components. These insights

would be instrumental in the development and enhancement of effective multi-stage isolation and cancellation strategies in FD communication systems.

B. CONTRIBUTIONS

This research focuses on exploring and developing a metamaterial absorber structure, designed to enhance Tx-Rx isolation in large-scale arrays capable of FD mMIMO applications, without necessitating any alterations to the existing antenna designs. Utilizing realistic simulations and experimental measurements, our goal is to present a comprehensive methodology for designing the metamaterial absorber structures and to showcase its potential to significantly reduce near-field SI with negligible impact on the far-field beamforming performance. Furthermore, a simple and strategic Tx-Rx joint beamforming isolation improvement mechanism is implemented to further mitigate the far-field SI in a very low near-field SI scenario. It serves to highlight the importance of the absorber structure in overcoming the challenges of near-field coupling, as well as in enhancing overall beam-level isolation performance. To our knowledge, this work is the first work that investigates the metamaterial absorber with beam-level isolation in FD mMIMO. The main contributions of this work are summarized as follows:

- **Metamaterial absorber for FD mMIMO:** A dual-layer metamaterial absorber is developed for our 8×8Tx/8×8Rx large-scale antenna arrays capable of the FD mMIMO. The realistic simulation illustrates a power absorption ratio of more than 99.8%. In experimental measurements conducted with a 20 MHz modulated signal in the anechoic chamber, the absorber significantly enhanced Tx-Rx isolation. On average,[1] an antenna element isolation improvement of 17.5 dB is observed, with the closest Tx-Rx element pairs achieving an isolation of 65.4 dB. Moreover, the absorber has contributed to an average improvement of 18.6 dB in Tx-Rx beam-level isolation in near-field dominant SI scenarios, with the largest isolation improvement of 42.0 dB. An average beam isolation of 79.2 dB with the best beam isolation of 104.4 dB is achieved, underscoring the absorber's ability to mitigate the near-field SI.

- **Experimental studies of absorber-assisted angular-perturbation beamforming isolation:** Experimental investigations on the correlation between the near-field and far-field dominant SI scenarios and the downlink and uplink beam directions are conducted. The results highlight the critical role of absorber structures in overcoming the bottleneck presented by near-field dominant SI in beam-level isolation design. To enhance the total isolation performance in scenarios with very low near-field SI, we implemented an angular-based

approach for Tx-Rx beam isolation improvement. Incorporating a simple steering angle perturbation of $2°$ in a 3dB-beamwidth search range with the proposed absorber structure, an average beam-level isolation of 90.8 dB is achieved within a downlink/uplink steering range between $-48°$ to $48°$. Across 49 test cases, all the beam-level isolation is better than 70.8 dB and more than half the amount of the Tx/Rx beam pairs can achieve an isolation level better than 90 dB.

- **Metamaterial absorber impacts on the beamforming performance:** Experimental measurements were conducted to assess the impacts of the introduction of the metamaterial absorber on the far-field beam patterns. These measurements align well with our simulation findings. Within the steering range of $-50°$ to $40°$, we observed marginal differences in beam patterns. The average variations in beam directivity, 3dB-beamwidth, 10dB-beamwidth, and normalized sidelobe level were found to be 0.2 dB, 0.8 degrees, 0.9 degrees, and 0.9 dB, respectively. These results suggest that the addition of an absorber, positioned λ_0 away from the Tx antenna array, exerts a negligible impact on the far-field beam pattern in the beamforming. This finding is essential for ensuring the effectiveness of the absorber on near-field coupling mitigation without compromising the integrity of the far-field beam pattern in the beamforming process.

C. ORGANIZATION

The observations outlined previously inspired the development of a metamaterial absorber to our 8×8Tx/8×8Rx FD mMIMO testbed. This paper details the process from simulations to experimental measurements, focusing on improving the Tx-Rx antenna isolation with the absorber structure. We investigate the effects of absorber positioning on absorption efficiency and examine how the absorber influences beam patterns and isolation improvement across various Tx/Rx beam angle combinations. The rest of the paper is structured as follows. Section II delves into the system models and SI channels employed in our study, providing the theoretical foundation for our research. Section III outlines the design process of the metamaterial absorber element. It includes simulation results demonstrating the absorber's effectiveness relative to its location and mounting position. Section IV introduces the fabricated absorber prototype integrated into our FD mMIMO testbed. We present experimental measurements conducted in an anechoic chamber, focusing on isolation improvement in near-field dominant SI scenarios. This section also explores the impact of the absorber structure on the beamforming performance of a sample 1×8 sub-array. Section V presents our investigation into combining absorber technology with angular-perturbation-based methods to enhance total beam isolation. We discuss the effectiveness of this approach in scenarios dominated by near-field and far-field SI components, highlighting the necessity of the absorber structure in guaranteeing the total beam isolation performance. Section VI concludes the paper,

---

[1]This study utilizes geometric means to characterize the average mutual coupling or isolation level, as the mutual coupling value represents a ratio of the received power to the transmitted power.
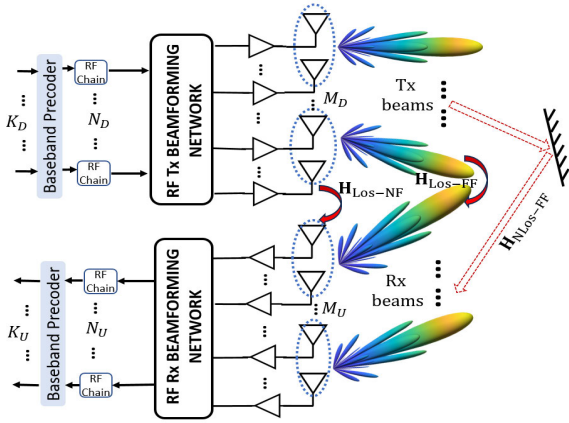
FIGURE 1. Proposed FD mMIMO system model.

summarizing our findings and suggesting future work in this area.

D. NOTATION AND COORDINATES

In the presentation, the antenna array is placed in the $xy-$ plane and the main radiation direction is perpendicular to the array plane (along the z-axis). This orientation corresponds to $\theta = 0°$ and $\psi = 90°$. Consequently, the θ angle plane aligns with the yz-plane. The following notations are used throughout this paper. Boldface lower-case and upper-case letters denote column vectors and matrices, respectively. $()^T$, $()^H$ and $\|.\|$ represent the transpose, Hermitian transpose, and the 2-norm of a vector or matrix, respectively. $\mathbf{I}_k$ denotes the $k \times k$ identity matrix. We use $x_k \sim \mathcal{CN}(0, \sigma^2)$ when x_k is a complex Gaussian random variable with zero-mean and variance σ^2.

II. SYSTEM MODEL

In our study, as depicted in Fig. 1, we focus on a single-cell FD mMIMO system designed for simultaneous downlink (DL) and uplink (UL) transmission. The base station (BS) comprises Tx and Rx antenna arrays with M_D and M_U antenna elements, respectively. The BS concurrently, operating in FD mode, serves K_D DL and K_U UL users. Meanwhile, the users, typically constrained by limited power and restricted signal processing capabilities, operate in HD mode.

To harness the benefits of beamforming isolation in large-scale arrays without incurring the drawbacks of extensive hardware complexity, a two-stage hybrid beamforming (HBF) design is adopted. It can be split into RF Tx/Rx beamforming, which focuses on the Tx/Rx beam direction management through phase shifters, and digital Baseband (BB) precoder/combiner, which processes the signal in the digital domain to maximize signal quality and efficiency. A low number of RF chains are used to connect the two stages, which can significantly reduce hardware complexity and cost compared with the fully digital approach. In the FD mMIMO system, the DL signal undergoes processing through a BB precoder $\mathbf{B}_D \in \mathbb{C}^{N_D \times K_D}$ and an RF beamformer

$\mathbf{F}_D \in \mathbb{C}^{M_D \times N_D}$. The number of RF chains, N_D, satisfies $K_D \leq N_D \ll M_D$. Similarly, the UL signal received at the BS passes through an RF beamformer $\mathbf{F}_U \in \mathbb{C}^{N_U \times M_U}$ and a BB combiner $\mathbf{B}_U \in \mathbb{C}^{K_U \times N_U}$, utilizing $K_U \leq N_U \ll M_U$ RF chains. The DL channel matrix, $\mathbf{H}_D \in \mathbb{C}^{K_D \times M_D}$, comprises channel vectors $\mathbf{h}_{D,k} \in \mathbb{C}^{M_D}$ for each DL user. Similarly, the UL channel matrix, $\mathbf{H}_U \in \mathbb{C}^{M_U \times K_U}$, includes channel vectors $\mathbf{h}_{U,k} \in \mathbb{C}^{M_U}$ for UL users. The SI channel matrix $\mathbf{H}_{SI} \in \mathbb{C}^{M_U \times M_D}$ arises due to FD transmission, coupling between Tx and Rx antennas at the BS.

For DL transmission, the BS transmits signal vector $\mathbf{s}_D = \mathbf{F}_D\mathbf{B}_D\mathbf{d}_D \in \mathbb{C}^{M_D}$, where $\mathbf{d}_D \in \mathbb{C}^{K_D}$ is the DL data signal vector, adhering to $\{\mathbf{d}_D\mathbf{d}_D^H\} = \mathbf{I}_{K_D}$. The received DL signal vector can be expressed as

$$\mathbf{r}_D = \underbrace{\mathbf{H}_D\mathbf{F}_D\mathbf{B}_D\mathbf{d}_D}_{\text{Desired Signal}} + \underbrace{\mathbf{H}_{IUI}\mathbf{d}_U}_{\text{IUI}} + \underbrace{\mathbf{n}_D}_{\text{Noise}}, \qquad (1)$$

where the matrix $\mathbf{H}_{IUI} \in \mathbb{C}^{K_D \times K_U}$ is the inter-user interference (IUI) channel. The $\mathbf{H}_{IUI}\mathbf{d}_U \in \mathbb{C}^{K_D}$ represents the IUI, indicating the interference between downlink and uplink users who are sharing the same time/frequency slots.

Similarly, the UL received signal at BS can be written as

$$\mathbf{r}_U = \underbrace{\mathbf{B}_U\mathbf{F}_U\mathbf{H}_U\mathbf{d}_U}_{\text{Desired Signal}} + \underbrace{\mathbf{B}_U\mathbf{F}_U\mathbf{H}_{SI}\mathbf{F}_D\mathbf{B}_D\mathbf{d}_D}_{\text{SI}} + \underbrace{\mathbf{n}_U}_{\text{Modified Noise}},$$

$$(2)$$

where $\mathbf{d}_U \in \mathbb{C}^{K_U}$ is the UL data signal vector, such that $\{\mathbf{d}_U\mathbf{d}_U^H\} = \mathbf{I}_{K_U}$. $\mathbf{n}_D$ and $\mathbf{n}_U$ are complex circularly symmetric Gaussian noise vectors for the DL and UL, respectively.

The beam steering directions for DL (UL) are defined by Azimuth and Elevation angles, denoted as $\theta_D(\theta_U)$ and $\psi_D(\psi_U)$, respectively. For this study, we simplify our model to serve a single UL user and a single DL user, i.e., $K_D = K_U = 1$, with two uniform linear arrays (ULAs). The downlink and uplink beamformer, $\mathbf{F}_D$ and $\mathbf{F}_U$, are constructed with phase shifters and uniform magnitudes, which focus on beam steering in Azimuth directions θ_D and θ_U with constant constant elevation angles $\psi_D = \psi_U = 90°$. Then, the Tx and Rx RF beam steering vectors can be expressed as follows,

$$\begin{aligned}\mathbf{F}_D(\theta_D) \\ = \frac{1}{\sqrt{M_D}}[\quad 1, e^{-j2\beta d_0 \sin(\theta_D)}, \dots, e^{-j\beta(M_D-1)d_0 \sin(\theta_D)}]^T,\end{aligned}$$

$$(3)$$

$$\begin{aligned}\mathbf{F}_U(\theta_U) \\ = \frac{1}{\sqrt{M_U}}\quad [1, e^{j2\beta d_0 \sin(\theta_U)}, \dots, e^{j\beta(M_U-1)d_0 \sin(\theta_U)}],\end{aligned}$$

$$(4)$$

where the $\beta = 2\pi/\lambda_0$ is the propagation phase constant and d_0 is the separation distance between two neighbouring antenna elements.

In FD mMIMO systems, UL transmissions primarily encounter two types of interference: multi-user interference (MUI) from multiple UL users and significant SI due to the

concurrent operations of the Tx and Rx at the BS. Illustrative results in [38], [40], and [41] have demonstrated that a synergistic design of $\mathbf{B}_U$ and $\mathbf{F}_U$ for the UL can effectively mitigate the MUI in the UL. Consequently, as elaborated in equation (2), the excessive in-band SI emerges as the predominant bottleneck affecting UL performance in FD communications. To attain UL detection performance in FD systems comparable to HD systems, minimizing SI, ideally to levels below thermal noise, is necessary. The SI channel encompasses both near-field and far-field components and can be expressed as

$$\mathbf{H}_{SI} = \underbrace{\mathbf{H}_{\text{Los}-\text{NF}}}_{\text{Near-field Coupling}} + \underbrace{\mathbf{H}_{\text{Los}-\text{FF}} + \mathbf{H}_{\text{NLos}-\text{FF}}}_{\text{Far-field Coupling}}. \quad (5)$$

Given the proximity of the Tx and Rx antennas, the predominant near-field SI components typically follow a LoS path and are denoted by $\mathbf{H}_{\text{LoS}-\text{NF}} \in \mathbb{C}^{M_U \times M_D}$. To minimize the $\mathbf{H}_{\text{LoS}-\text{NF}}$, antenna isolation design is implemented as the first line aiming to prevent coupling waves generated in potential interference directions from being captured by the local Rx. In our sample $8 \times 8\text{Tx}/8 \times 8\text{Rx}$ FD mMIMO prototype, Tx-Rx antenna isolation is initially achieved through cross-polarization and physical separation between the Tx and Rx antennas [36]. To further improve the isolation performance, in this study, a metamaterial absorber is proposed and strategically placed within a distance of λ_0 from the transmitter. The absorber is specifically focused on absorbing and dissipating potential coupling waves, to reduce the strength of the near-field LoS component, $\mathbf{H}_{\text{LoS}-\text{NF}}$, and consequently, suppressing the $\mathbf{H}_{SI}$.

In contrast, the far-field coupling includes both LoS and NLoS components, represented by $\mathbf{H}_{\text{LoS}-\text{FF}} \in \mathbb{C}^{M_U \times M_D}$ and $\mathbf{H}_{\text{NLoS}-\text{FF}} \in \mathbb{C}^{M_U \times M_D}$, respectively. The $\mathbf{H}_{\text{NLoS}-\text{FF}}$ typically results from environmental reflections of radiation waves. In environments characterized by low reflection properties, the influence of $\mathbf{H}_{\text{NLoS}-\text{FF}}$ is considerably diminished. Such environments include simulations conducted under perfect electric (perfect-E) boundary conditions, experiments within anechoic chambers outfitted with efficient RF absorbers, and outdoor settings like rural areas or open fields. In these settings, the reduced presence of reflective surfaces and obstacles significantly lessens the impact of NLoS components in far-field coupling.

Additionally, due to the separation between our sample $8 \times 8\text{Tx}$ and $8 \times 8\text{Rx}$, which is approximately $2.5\lambda_0$ edge-to-edge, the far-field beam interaction also contributes to the total SI. Therefore, by confining and controlling the wave propagation, beamforming plays a pivotal role in mitigating the LoS far-field component, $\mathbf{H}_{\text{LoS}-\text{FF}}$, in the FD communications. Specifically, the direct interaction between Tx and Rx beams, represented by the Tx and Rx gains in specific directions, can be strategically managed through far-field beam steering techniques. As demonstrated in [36], steering the Rx beam towards the radiation nulls or low gain directions of the Tx beam is instrumental in reducing Tx-Rx MC. The approach entails introducing
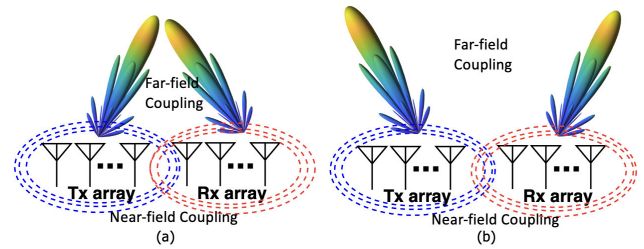

FIGURE 2. Far-field/Near-field coupling when Tx/Rx beams steering (a) towards each other (b) away from each other.

beam angle perturbations to align the Rx beam angles with the Tx radiation nulls. Such strategic alignment focuses on mitigating the beamforming-modified far-field LoS SI, $\mathbf{F}_U \mathbf{H}_{\text{LoS}-\text{FF}} \mathbf{F}_D$. Consequently, this leads to a decrease in the magnitude of $\mathbf{F}_U \mathbf{H}_{SI} \mathbf{F}_D$, thereby enhancing the overall performance of the FD system.

Two representative scenarios of the Tx/Rx beam directions against the MC scenarios are illustrated in Fig. 2. In the first scenario, where the Tx and Rx beams are directed across each other, i.e., $\theta_D > 0°$ and $\theta_U < 0°$, a relatively stronger far-field interaction between the two beams can be observed. Conversely, in the second scenario, the beams are steered away from each other, i.e., $\theta_D < 0°$ and $\theta_U > 0°$, and avoid a strong interaction between the Tx and Rx main lobes. Here, the far-field interaction between the Tx/Rx main lobes is comparatively weaker, which leads to a near-field dominant SI scenario. The detailed discussions of the isolation improvement strategies in different beam interaction scenarios will be presented in Section V.

III. METAMATERIAL ABSORBER DESIGN
A. METAMATERIAL ABSORBER ELEMENT STRUCTURE
The proposed dual-layer metamaterial absorber unit cell is depicted in Fig. 3. Two identical Split Resonator Dual-Ring (SRDR) patch circuits are printed symmetrically on the bottom side of the lower FR-4 dielectric substrate and on the top side of the higher FR-4 dielectric substrate. The employed FR-4 dielectric material has a dielectric constant $\epsilon_r = 4.6$. The SRDR structure is strategically designed to be integrated with our previously proposed $8 \times 8\text{Tx}/8 \times 8\text{Rx}$ array prototype for FD mMIMO operation. The copper ground plane in the middle of the sandwiched construction is shared by the two SRDR circuits. With concentric split resonators, the SRDR structure affords greater flexibility in manipulating the effective permittivity and the effective permeability. This is achieved by introducing adjustable gaps between the central and outer split rings and extending the length of metallic strips. The surface capacitance controlled by the gaps between and inside the metallic circuits and the dielectric material between the top circuits and ground plane contributes to the modification of the metamaterial's ability to store and respond to electric fields. Consequently, the effective permittivity of the metamaterial can be finely tuned. For instance, reducing the gap between conductors leads to increased capacitance, thereby enhancing
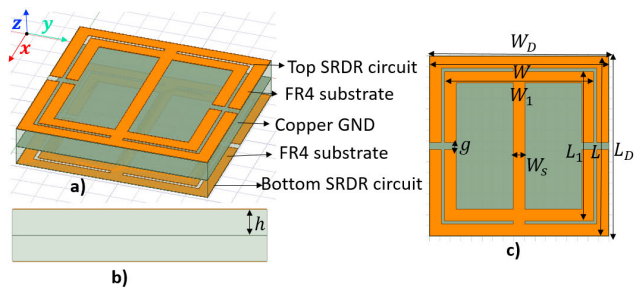
FIGURE 3. Metamaterial absorber element structure (a) layer diagram; (b) side view; (c) Top view.

TABLE 2. Dimensions of the proposed metamaterial absorber element.

Label	Description	Value (mm)
W	outer layer circuit width	16.9
L	outer layer circuit length	16.9
W_D	FR4 dielectric substrate width	17
L_D	FR4 dielectric substrate length	17
h	FR-4 substrate thickness	1.7
W_1	inner layer circuit width	14.1
L_1	inner layer circuit length	14.1
W_s	copper conductor circuit width	1.1
g	circuit gap width	0.7

the structure's ability to interact with and store electrical energy. This enhanced interaction, due to increased electrical energy storage capacity, facilitates an apparent adjustment in the metamaterial's effective permittivity. In addition, the inductance, determined by the length and geometry of the conducting strips in the meta-cell and generated by the current flowing through these adjacent cells, controls the metamaterial magnetic response. An increase in inductance, achieved through longer and twisted conducting paths that enhance magnetic field linkage, results in a higher effective permeability.

The metamaterial absorber cells shown in Fig.3 are designed to connect edge-to-edge, forming a two-dimensional array that extends along both the $x-$ and $y-$axes. The overall size of the absorber structure is determined by the count of SRDR absorber elements along the $x-$axis (N_x) and the $y-$axis (N_y). Ansys high-frequency structure simulator (HFSS) is used in the design process to adjust and optimize the surface impedance of the absorber units using Floquet port and primary/secondary periodic boundary conditions. The suggested SRDR unit element dimensions are shown in Table 2. The absorber structure power absorption ratio (ρ) can be found via the S-parameter simulation, where $\rho = 1 - |S_{11}|^2$. The simulated power reflectivity and absorption ratio are shown in Fig. 4. The simulation results indicate that more than 99.8% of power is absorbed at 3.49 GHz. This high absorption power ratio ensures effective mitigation of near-field coupling waves, with a considerable amount of incident coupling wave travelling from the Tx to the Rx antennas being absorbed and dissipated in the absorber structure. Moreover, the absorber surface power reflection of less than 0.2% also contributes to reduced interference to the transmitting signals, preserving the integrity of the original beam patterns. Details of the absorber impact on the array
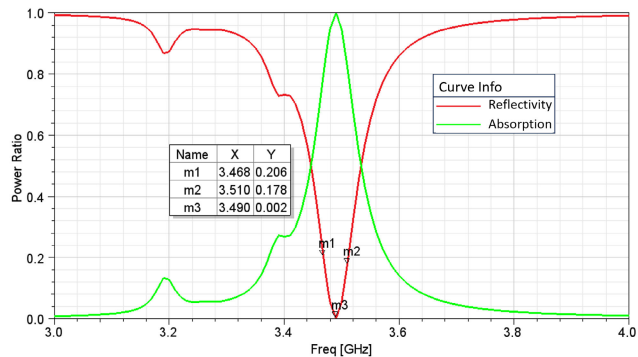

FIGURE 4. Power absorption and reflection of the proposed metamaterial absorber structure (simulation results).
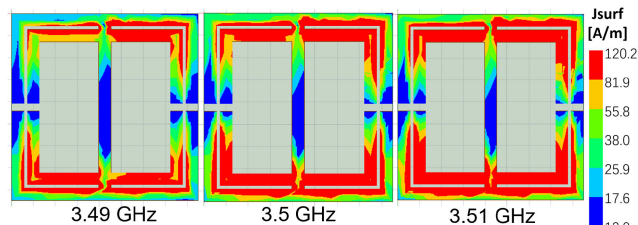

FIGURE 5. Surface current distribution of the metamaterial absorber at 3.49GHz, 3.5GHz, and 3.51GHz (simulation results).

beamforming will be further investigated via simulations and measurements.

The distribution of surface current on metamaterial absorbers also serves as an important indicator of the interaction strength between coupling waves and the metamaterial structure. The surface current distribution at three sample operating frequencies 3.49 GHz, 3.5 GHz, 3.51 GHz are illustrated in Fig. 5. Across the target frequency bandwidth, a consistent distribution of high-strength surface currents can be observed. This consistent induction of strong surface currents indicates that a substantial portion of the incident electromagnetic waves effectively interacts with and couples to the periodic SRDR structures. The notable excitation of surface current within these frequencies indicates that the metamaterial is in strong resonance with the incoming electromagnetic waves, facilitating an effective absorption of the coupling waves.

B. ABSORBER LOCATION EFFECTS ON ISOLATION IMPROVEMENT

The size of the absorber structure determines the path of the undesired leakage waves interacting with the absorber structures. A larger absorber structure typically exhibits stronger interactions with leakage waves, due to the increased number of pathways available for absorption. Therefore, a higher isolation enhancement can be achieved. For effective absorption and isolation, the absorber's dimensions should be comparable to the wavelength of the electromagnetic waves it is designed to interact with. Typically, effective absorbers are at least half a wavelength to several wavelengths in size in the dimension of interest. For an affordable iterative simulation
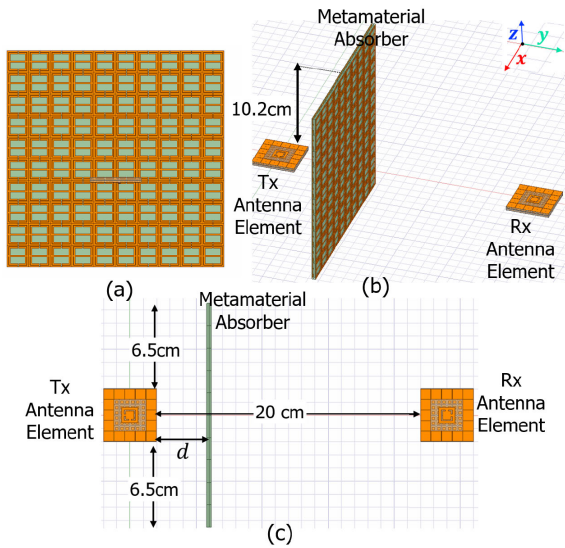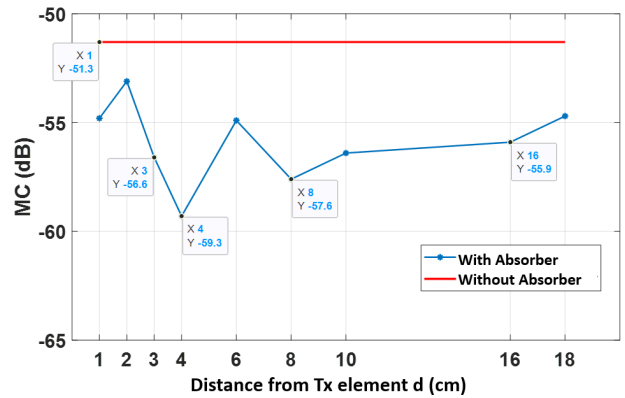
FIGURE 6. (a) 10 × 10 Metamaterial absorber, (b) perspective view, and (c) top view of the MC simulation setup with Tx/Rx antenna elements and absorber.

FIGURE 7. MC between Tx and Rx antennas versus *d* (simulation results).

TABLE 3. Tx/Rx MC without and with absorber at different *d* (simulation results).

Tx/Rx arrays	Absorber to Tx distance (d)	Avg. Elem. Tx-Rx MC(dB)	Avg. MC Diff. (dB)	Max Elem. Tx-Rx MC(dB)	Max MC Diff. (dB)
4x4	no ABS	-50.9		-38.1	
	4 cm	-60.1	9.2	-48.4	10.3
	8 cm	-58.1	7.2	-46.6	8.5
8x2	no ABS	-46.8		-38.0	
	4 cm	-55.5	8.7	-45.9	7.9
	8 cm	-54.9	8.1	-44.3	6.3

time[2] and the effectiveness of the isolation enhancement, a metamaterial absorber with 10 × 10 (17 cm × 17 cm) proposed meta-cell structures, shown in Fig. 6 (a), is used in the HFSS simulation. The absorber has a width of 17 cm, which is approximately equivalent to two wavelengths, ensuring sufficient interaction with the leakage near-field coupling waves. As depicted in Fig. 6 (b) and (c), the absorber is vertically positioned between the Tx and Rx antennas, which are spaced 20 cm apart, edge-to-edge. The absorber extends 6.5 cm beyond the edge of the antennas in both $+x$ and $-x$ directions and is 10.2 cm above the surface of the patch antenna. The 6.8 cm absorber structure lower than the antenna surface can help mitigate the back leakage waves from the Tx element toward the Rx element. Only the Tx antenna (on the left) is excited at 3.5 GHz. The separation distance between the absorber and the Tx antenna (d) varies from 1 cm to 18 cm to find the best location of the absorber.

The simulation results are shown in Fig. 7. The findings show that the absorption effectiveness can be impacted by the absorber location. When 2 cm$< d <$18 cm, a Tx-Rx element MC level lower (better) than -55 dB can be achieved. When comparing the Tx-Rx element MC with the scenario without the absorber structure, an 8 dB lower MC level can be attained when the absorber is at a distance of 4 cm ($d \approx \lambda_0/2$) and 6.3 dB isolation improvement is attained when the absorber is at 8 cm distance ($d \approx \lambda_0$). The effectiveness of the absorber diminishes when its distance from the transmitter exceeds the absorber's optimal operation range, which is determined by its resonant wavelength. Beyond these distances, a notable decline in isolation enhancement performance can be observed due to weaker resonant effects

----

[2]The realistic simulations used our proposed intricate dual-layer EBG-slotted antenna element demands high computational resources. The separation distance between the Tx-Rx antennas is kept at 20 cm which is consistent with our 8 × 8Tx/8 × 8Rx antenna array prototype.

at the absorber surface and reduced interactions between the near-field coupling paths and the absorber structure.

To further investigate the absorber structure enhancement on the Tx-Rx element isolation level, two 16-element antenna arrays (4 × 4 or 8 × 2) with the proposed Tx and Rx antenna elements separated by 20 cm edge-to-edge are simulated. The absorber structure is extended along the $\pm x-$ axis, to keep 6.5 cm longer than the antenna array on each side. The results are summarized in Table 3.

Placing an absorber at 4 cm and 8 cm can lower (improve) the Tx-Rx element MC by 9.2 dB and 7.2 dB on average, respectively, when two 4 × 4 arrays are used, and by 8.7 dB and 8.1 dB on average, respectively, when two 8 × 2 arrays are used. The average difference between the Tx-Rx element MC is less than 2 dB when placing the absorber at 4 cm and 8 cm from the Tx array. When comparing the worst MC pairs, adding the absorber 4 cm or 8 cm from the Tx array leads to an improvement difference of 1.8 dB and 1.6 dB, respectively, when two 4 × 4 arrays or 8 × 2 arrays are used.

In the FD mMIMO design, the absorber's impact on array beamforming performance is also essential to be considered. To optimize beamforming and beam-level isolation without compromising beam steerability, the absorber must not obstruct the beam's path within its effective steering range. Consequently, we chose $d = 8$ cm for the absorber in our design to prevent beam propagation blockage in the beamforming.

C. ABSORBER MOUNTING EFFECTS ON ISOLATION IMPROVEMENT

Given the computational resource limitation, particularly in terms of Random Access Memory (RAM), and processing
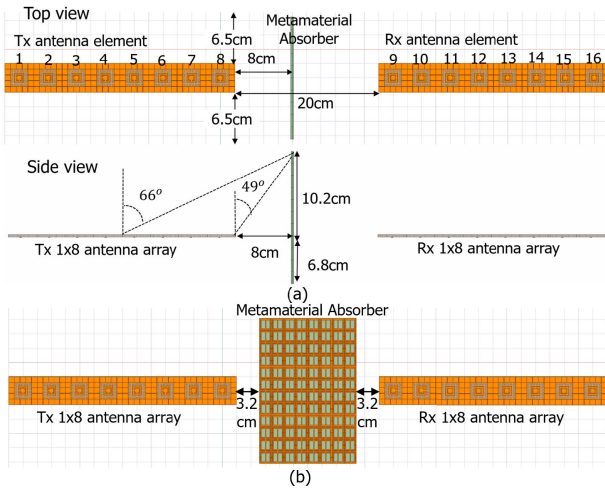
FIGURE 8. Simulation setups and antenna element indices with (a) vertically-mounted absorber (top and side views); (b) horizontally-mounted absorber (top view).

time of the simulation of the whole $8 \times 8\text{Tx}/8 \times 8\text{Rx}$ arrays, we use two sample orthogonally-polarized 1×8 arrays with the proposed Tx and Rx antenna element structures, operating at 3.5 GHz and separated by 20 cm edge-to-edge. The simulation setups with the antenna element indices are shown in Fig. 8 (a) and (b) for vertically and horizontally mounted absorbers, respectively. Our investigation focuses on studying the Tx-Rx element/beam MC and beamforming performance under two different absorber mounting scenarios.

1) ABSORBER MOUNTING AND TX-RX ELEMENT MC
a: HORIZONTALLY-MOUNTED ABSORBER
By comparing Fig. 9 (a) and Fig. 9 (b), the average Tx-Rx element MC is lowered (improved) from -47.3 dB to -57.4 dB, where an average 10.1 dB lower (better) MC level is achieved by adding the absorber. Fig. 9 (b) demonstrates that the horizontal absorber's effectiveness increases as the Tx and Rx elements move further apart. This enhancement, particularly evident in the lower-left quadrant of the plot, is attributed to stronger surface wave coupling interactions with the horizontally mounted absorber at greater distances (order of a half-wavelength or more). The rise in path loss attributed to the increased distance between elements also contributes to the reduction in MC between the Tx and Rx. The highest (worst) Tx-Rx element pair MC level is reduced from -38.9 dB to -42.7 dB, equivalent to a 3.8 dB improvement, which can be a potential limitation in the beam MC and isolation effectiveness when the antenna arrays are employed.

b: VERTICALLY-MOUNTED ABSORBER
Comparison between Fig. 9 (a) and Fig. 9 (c) reveals a notable Tx-Rx isolation improvement. An average reduction of 9.2 dB in the Tx-Rx element MC level can be achieved, and an average MC level of -56.5 dB can be achieved. Across all the 64 Tx-Rx element pairs, the MC level is consistently lower than -51.9 dB. Furthermore, the

worst-case (highest) MC level is reduced (improved) by 13.0 dB compared to the scenario without an absorber structure. This improvement is 9.2 dB greater than the case with a horizontally mounted absorber. As the Tx elements and Rx elements move closer to each other, a higher near-field MC intensity is suffering. Therefore, it can also be observed that as the Tx and Rx element pairs move close to the absorber structure (e.g., Tx element 8 and Rx element 9), a more considerable isolation improvement can be achieved. An average isolation improvement of 14.8 dB and 19.4 dB can be achieved between Tx-elem-8 and any Rx antenna elements and Rx-elem-9 and any Tx antenna elements, respectively. Furthermore, the effective attenuation of near-field LoS coupling components between the Tx and Rx significantly reduces the correlation between their distance and the MC level.

2) EFFECTS OF THE ABSORBER MOUNTING ON THE BEAM MC
The MC between the Tx and Rx arrays at various Tx and Rx beam steering angles θ_D and θ_U can be calculated through a weighted sum of each individual Tx-Rx antenna element pair's complex MC values and can be expressed as

$$S_b(\theta_D, \theta_U) = \sum_{j=9}^{16} \sum_{i=1}^{8} w_i^*(\theta_D) w_j^*(\theta_U) S_{ji}, \qquad (6)$$

where S_{ji} is the complex S-parameter that represents the coupling between the Tx antenna element i and the Rx antenna element j in the arrays. $w_i(\theta_D)$ and $w_j(\theta_U)$ are the complex steering weights for the Tx element i and Rx element j at the Tx beamforming angle θ_D and Rx beamforming angle θ_U in the Azimuth plane. The estimated MC values between Tx 1×8 and Rx 1×8 arrays for the three cases at 3.5 GHz are shown in Fig. 10. Both the Tx and Rx beams are steering from $-50°$ to $50°$ with a $2°$ step size. Therefore, a total of $51 \times 51 = 2601$ beamforming MC combinations are investigated.
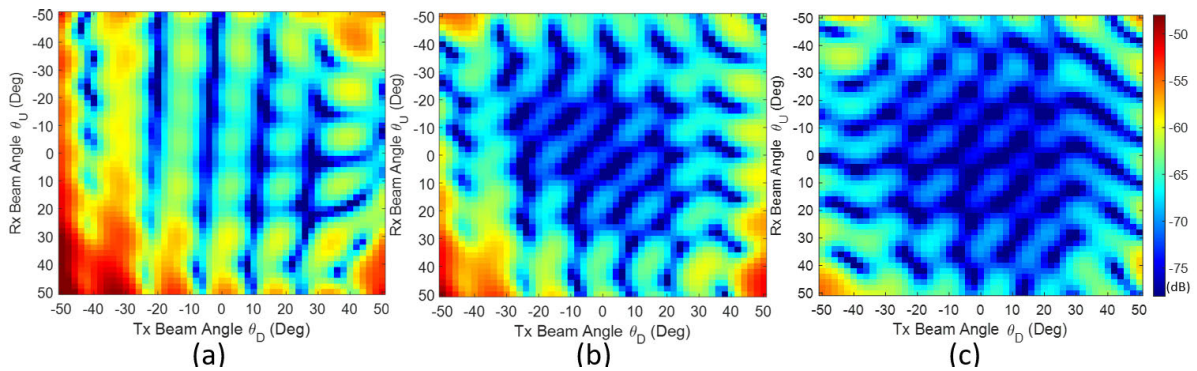
a: HORIZONTALLY-MOUNTED ABSORBER
Without the absorber structure, the average beamforming MC level across the 2601 beam combinations is -64.2 dB as shown in Fig. 10 (a). Incorporating the horizontally-mounted absorber reduces the average beam MC to -68.1 dB, representing an improvement of 3.9 dB on average. This modest enhancement can be attributed to the reduced contribution of surface wave coupling to the total SI intensity when the elements are configured into directional beams.

It can be observed that when beams are steering away from each other (left-bottom quarter of the plot, i.e., $\theta_D \in [-50°, -2°]$ and $\theta_U \in [2°, 50°]$), the absorber structure is more effective, with an average improvement of around 6 dB. When the Tx beam steers towards the Rx array, the absorber structure becomes less effective, and an average of 3.1 dB (right-top quarter of the plot, i.e., $\theta_D \in [2°, 50°]$ and $\theta_U \in [-50°, -2°]$).
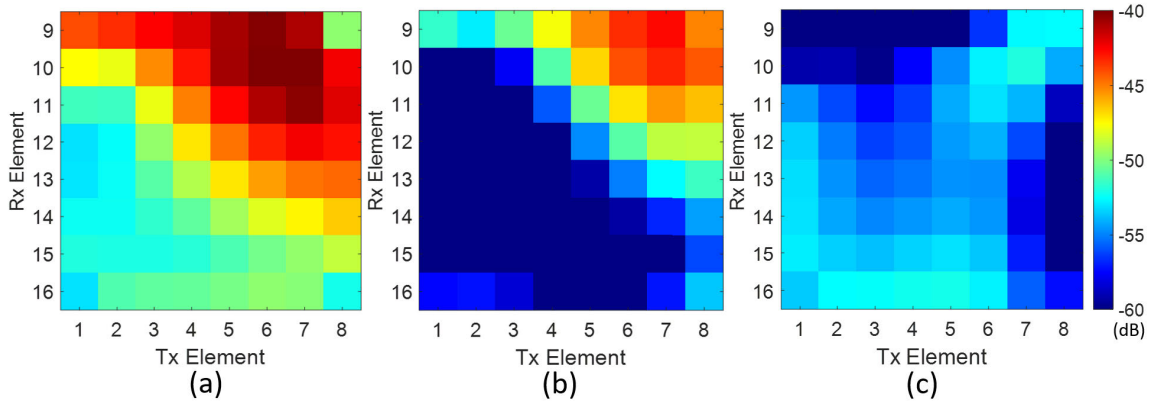
FIGURE 9. Tx-Rx antenna element MC magnitude maps in two 1 × 8 arrays at 3.5 GHz (a) without absorber; (b) with horizontally-mounted absorber; (c) with vertically-mounted absorber (simulation results).

FIGURE 10. Tx-Rx beam MC magnitude maps with 1 × 8 antenna arrays at 3.5Hz (a) without absorber; (b) with horizontally-mounted absorber; (c) with vertically-mounted absorber (simulation results).

b: VERTICALLY-MOUNTED ABSORBER

As shown in Fig. 10 (c), with the vertically-mounted absorber structure, an average beam MC of -71.1 dB can be achieved, which is 6.9 dB lower (better) than the no-absorber case. A more dense amount of high-isolation Tx/Rx beam angle pairs, which results in a higher fraction of high-isolation (θ_D, θ_U) pairs in the steering range, can be observed in Fig. 10 (c). All 2601 beamforming combinations have an MC lower than -55 dB. The result indicates that the vertically mounted absorber reduces (improves) the highest beam MC by 11.5 dB. A larger isolation improvement can be observed when steering Tx and Rx beams away from each other (i.e., $\theta_D \in [-50°, -2°]$ and $\theta_U \in [2°, 50°]$), with an average MC of 10.8 dB lower.

When comparing Fig. 10 (b) and (c), vertically mounting the absorber leads to an average of 3 dB higher isolation improvement compared with the horizontal case. Additionally, the highest (worst) beam-level MC is constrained by the most severe Tx-Rx antenna element MC level. Notably, the worst beam MC is reduced by 6.6 dB, dropping from -48.4 dB to -55.0 dB when vertically mounting the absorber compared to the horizontal position.

The beam steering directions have a significant impact on the performance of the absorber. For both vertically and horizontally mounted absorbers, when the Tx and Rx beams are steered away from each other (i.e., $\theta_D \in [-50°, -2°]$ and

$\theta_U \in [2°, 50°]$), we observe a considerably higher isolation improvement. This is because, in such configurations, the far-field beam interaction diminishes, making the near-field coupling components more dominant and the absorber structure is specifically designed to address these near-field coupling waves. To get better beamforming isolation across all the (θ_D, θ_U) pairs, vertically mounting is used in our following simulations and measurements.

D. ABSORBER IMPACT ON BEAM PATTERN: SIMULATION RESULTS

The Tx 1×8 array with the configuration depicted in Fig. 8 (a) is simulated to assess the impact of a vertically-mounted absorber structure on beamforming performance. The simulated beam patterns with and without the vertically-mounted absorber structure at 3.5 GHz are illustrated in Fig. 11. The Tx 1×8 array is steering within the range $\theta_D \in [-50°, 50°]$. Without the absorber structure, an average directivity of 13.3 dB is achieved in the steering range. The 3dB- and 10dB-beamwidths are consistently narrower than 18 degrees and 32 degrees, respectively. The normalized sidelobe level is consistently lower than the main lobe peak level by 9.5 dB.

With the incorporation of the absorber, the resulting beam from the Tx 1×8 array exhibits slight variations. An average directivity difference of 0.3 dB, an average 3dB-beamwidth difference of 0.6 degrees, and an average beam peak direction
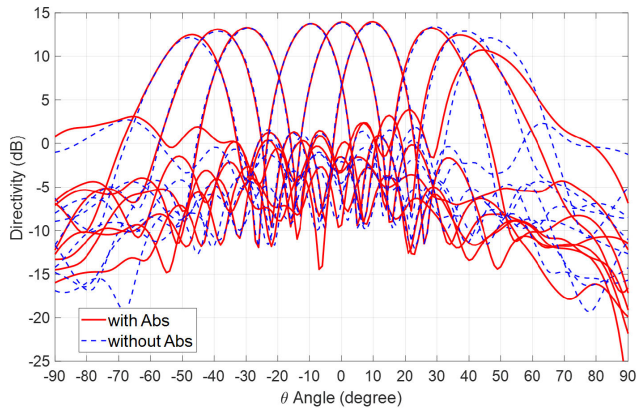
FIGURE 11. 1 × 8-array Tx beam pattern with and without the absorber at steering angle −50°, −40°, −30°, −10°, 0°, 10°, 30°, 40°, and 50° (simulation results).

variation of 0.9 degrees can be observed over the steering range from −50° to 50°.

The main lobes of the Tx 1 × 8 array with and without absorbers overlap with each other, and the difference between directivity and beamwidth is smaller than 0.4 dB, and 1 degree, respectively, in the range −50° to 40°. The slight beam pattern variation suggests that the introduction of the absorber, which is vertically mounted 8 cm from the Tx array, has a negligible effect on the array's beamforming performance and far-field beam patterns. The observation also indicates that the interaction between the absorber structure and the Tx radiation wave primarily occurs with the near-field coupling components. When $\theta_D \geq 50°$, the difference between the mainlobe peak and the sidelobe level decreases by 1.2 dB. As shown in Fig. 8 (a), at these larger steering angles, the absorber starts to impede the beam's propagation path, leading to a beam pattern degradation. The absorber intercepts the desired wave radiating in this direction that would otherwise contribute to the main lobe, diminishing antenna gain. This inadvertent interaction leads to an increase in the normalized side lobes and the main lobe beamwidth, diminishing the array directivity. Consequently, this can distort the intended radiation patterns of the antenna array.

IV. EXPERIMENTS WITH THE METAMATERIAL ABSORBER

A. AN 8 × 8TX/8 × 8RX ANTENNA ARRAY PROTOTYPE WITH METAMATERIAL ABSORBER

The 8 × 8Tx/8 × 8Rx antenna array prototype with the metamaterial absorber for FD mMIMO is shown in Fig. 12. The 8 × 8 Tx/Rx antenna arrays are positioned 20 cm apart. The entire Tx/Rx antenna-array prototype spans a total length of 84 cm and a width of 32 cm. The 10 × 27-element absorber prototype (Fig.13) is vertically mounted between Tx and Rx antenna arrays. Additionally, the metamaterial absorber prototype has relative dimensions similar to the absorber utilized in the simulation. Specifically, the absorber structure extends approximately one wavelength longer, or 8.95 cm, relative to the center of the edge element in the antenna array,
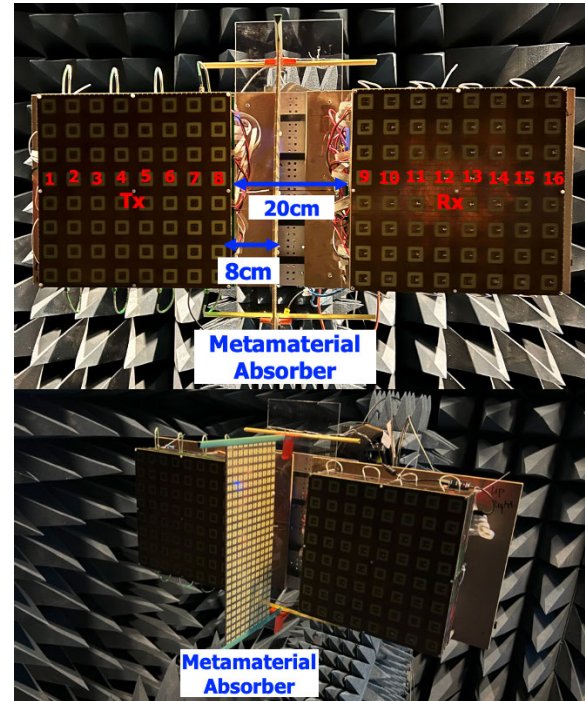
FIGURE 12. 8 × 8Tx/8 × 8Rx FD mMIMO array prototype with the metamaterial absorber (top: front-view with element and sub-array indices, bottom: perspective view).

or it is 6.95 cm longer than the array prototype at both the top and bottom sides. To effectively block and absorb the LoS leakage waves without hindering wave propagation within the array's effective steering range, the absorber includes a section that is 10.2 cm above the array surface. Furthermore, a part of the absorber extends 6.8 cm below the antenna surface, facilitating not only an easier installation but also ensuring efficient absorption and interaction with potential back leakage waves. Additionally, the absorber is positioned 8 cm away from the Tx array, ensuring optimal functionality in mitigating interference. Further details of the prototypes are briefly described in the following sections.

1) METAMATERIAL ABSORBER PROTOTYPE

An absorber prototype consisting of 10 × 27 SRDR metamaterial elements is fabricated, as shown in Fig. 13. The absorber has a total dimension of 45.9 cm × 17 cm × 0.35 cm (length × width × height). The prototype is 13.9 cm longer than the antenna array. FR-4 material with a dielectric constant (ϵ_r) 4.6 is used in the PCB manufacture.

2) CROSS-POLARIZED 8 × 8TX/8 × 8RX ANTENNA ARRAYS

To investigate the Tx-Rx antenna element and sub-array beamforming isolation performance with and without the absorber structure, the FD mMIMO prototype consists of an RF feeding network and a pair of cross-polarized 8×8Tx and 8×8Rx antenna arrays [36]. The antenna element is designed to operate over a 250 MHz bandwidth, covering the frequency range from 3.35 GHz to 3.6 GHz. A key feature of the antenna elements is the integration of dual-layer Electromagnetic
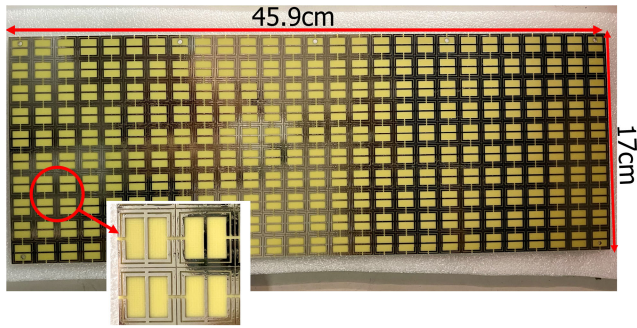
FIGURE 13. The 10 × 27-element metamaterial absorber prototype.

FIGURE 14. Measurement setup in the anechoic chamber.

Band Gap (EBG) structures. Incorporating EBG elements beneath the radiating patch significantly minimizes its size by 65% via inducing slow-wave propagation effects. Moreover, the upper periodic EBG layer functions as a band-pass filter, which suppresses the surface coupling wave and improves the inter-element isolation. As illustrated in [42], within the frequency range of 3.35 GHz to 3.6 GHz, the antenna element return loss is consistently better than 10 dB and the inter-element mutual coupling is better than -14.3 dB. To avoid the grating lobes in the beamforming, the separation distance between neighbouring antenna elements is set to 2.78 cm (0.32 λ_0 at 3.5 GHz) edge-to-edge or 4.00 cm (0.47 λ_0) center-to-center. The direction of the circular polarization (CP) is controlled by the relative location between the feeding point and the slot direction on the central radiating patch. The polarization of the Tx elements is adjusted to be right-handed CP (RHCP). Then, the Rx patch antenna is created by mirroring the Tx element structure, resulting in a left-hand CP (LHCP).

3) MEASUREMENT SETUP

The placement of the array prototype in the anechoic chamber is shown in Fig. 14. The chamber is equipped with the C-RAM SFC-48 absorber to minimize reflections and external interference and has a dimension of 6.1 m × 2.4 m × 2.4 m (length × width × height). For both results presented in Sections IV and V, the Spectrum Analyzer is used to take measurements of the receiving signal at the Rx antenna element/sub-array when a modulated NR-FR1-TM3.1 test signal with a 20 MHz bandwidth[3] (between 3.49 GHz and 3.51 GHz) and an output power of 10 dBm generated from a Vector Signal Generator (VSG) is sent from the Tx antenna element/sub-array. In the Tx-Rx element mutual coupling measurements, only a single Tx antenna element is used for transmitting the signal and only a single Rx antenna element is used as receiver in each measurement. We manually switched the cable between different Tx-Rx element pairs.

[3]This study concentrates on narrow-band scenarios, with a 20 MHz bandwidth, to circumvent issues related to frequency-dependent beam patterns and avoid the complexity in calculating frequency-specific weight factors.
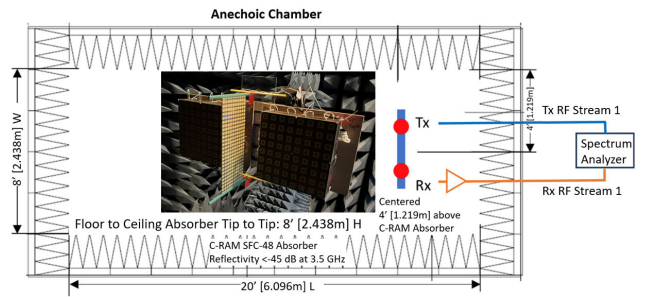
In the sub-array beam-level experiments, two sample sub-arrays, Tx/Rx 1 × 8, located at the center (fourth row of the Tx/Rx arrays) are used for the beamforming and isolation measurements as labelled in Fig. 12. On the Tx side, the signal undergoes initial splitting via a 1-to-8 power splitter before entering the beamforming network. Subsequently, the eight paths will be modulated by 8 digitally controlled 6-bit phase shifters. These phase shifters, controlled by a pre-calculated steering weight vector, facilitate the manipulation of the phase across 360 degrees with a fine step size of 5.625 degrees, ensuring precise beam direction control. Before the signal is fed to the antenna, the final stage RF amplifiers are employed to maximize transmitted power and compensate for the insertion loss of the system.

On the Rx side, each sub-array is directly connected to Low-Noise Amplifiers (LNAs) and then 8 digitally controlled 6-bit phase shifters. The high Tx-Rx isolation which contributes to a low received coupling signal necessitates the use of LNAs to enhance measurement sensitivity by boosting the signal-to-noise ratio (SNR). The signals from these eight paths are then combined through an 8-to-1 power combiner and fed into the Spectrum Analyzer.

Short coaxial cables and compact JSC connectors are used for interconnecting the components, all of which are arranged behind the antenna arrays for efficiency and convenience. The entire feeding network is controlled through two customized Serial Peripheral Interface (SPI) modules, one for the Tx beamformer and the other one for the Rx beamformer, which are integrated into Raspberry Pi 4. The beamforming vectors $\mathbf{F}_D(\theta_D)$ and $\mathbf{F}_U(\theta_U)$ for the Tx and Rx antenna sub-arrays are generated by a computer running a MATLAB-based beamforming program, which utilizes Equations (3) and (4). The computer interfaces with the SPI modules for control purposes and the Spectrum Analyzer for analysis purposes via USB cables. During each beam-pair measurement, the control signals are first updated on the SPI modules based on the $\mathbf{F}_D(\theta_D)$ and $\mathbf{F}_U(\theta_U)$. Subsequently, the readings from the Spectrum Analyzer, indicating the mutual coupling levels between the Tx and Rx antennas, are recorded.

B. MEASURED MUTUAL COUPLING BETWEEN TX AND RX ANTENNA ELEMENTS

The measurement results of Tx-Rx antenna elements, both with and without the proposed metamaterial absorber
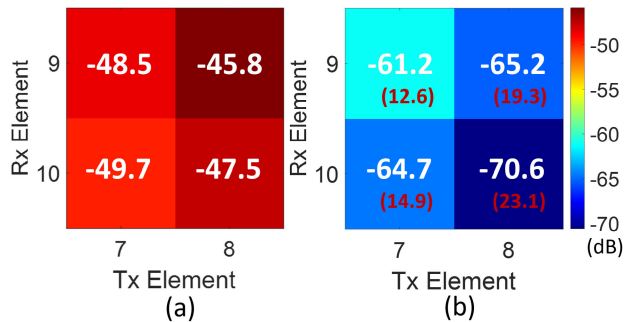
FIGURE 15. Tx-Rx antenna element MC magnitude maps in (dB) (a) without the absorber; (b) with the absorber (measured results).

FIGURE 16. Tx-Rx 1 × 8 arrays' beam MC magnitude maps in (dB) (a) without the absorber; (b) with the absorber (measured results).

structure, are illustrated in Fig. 15. The study focuses on Tx antenna elements 7 and 8, as well as Rx elements 9 and 10, which are the closest Tx/Rx antenna element pairs and most affected by the near-field MC, to assess the efficacy of the proposed absorber in isolation improvement, as labelled in Fig. 12. Only one of the Tx antenna elements is excited in each measurement.

As shown in Fig. 15 (a), without the absorber, the Tx-Rx antenna element MC level is -47.9 dB on average with an MC range from -49.7 dB to -45.8 dB. As the distance between Tx and Rx elements decreases, higher MC values are observed. For example, the MC between Tx-8 and Rx-9 is 3.9 dB higher than the farther element pair Tx-7 and Rx-10.

As illustrated in Fig. 15 (b), adding the absorber structure introduces an average reduction (improvement) of 17.5 dB in Tx-Rx antenna element MC, resulting in an average element MC of -65.4 dB. The Tx-Rx antenna element isolation improvement of the four Tx-Rx element pairs with and without the absorber is highlighted by the red values in Fig. 15 (b). The isolation enhancement is consistent across all four test cases, greater than 12.6 dB, with the highest improvement reaching 23.1 dB. The highest (worst) Tx-Rx element MC pair is -61.2 dB, with a reduction of 15.4 dB thanks to the absorber. Due to the effective suppression of near-field coupling waves by the absorber structure, the correlation between antenna element separation distance and MC levels is notably weakened.

The measured results show a similar absorber effectiveness change as the simulation results at similar relative locations. A significant isolation improvement can be seen as the Tx and Rx antenna element pairs become closer to the absorber structure. For instance, an MC improvement of -21.2 dB is obtained on average between Tx element 8 and the Rx element 9 and 10.

The EBG patches surrounding the tested sample Tx and Rx elements create a high surface impedance, which works as a band-stop filter. This impedance effectively mitigates and blocks the propagation of coupling waves in the direction parallel to the absorber structure, along the x−axis. Consequently, the near-field coupling along the y−axis, perpendicular to the absorber, becomes the predominant factor contributing to SI, leading to a more considerable isolation improvement.
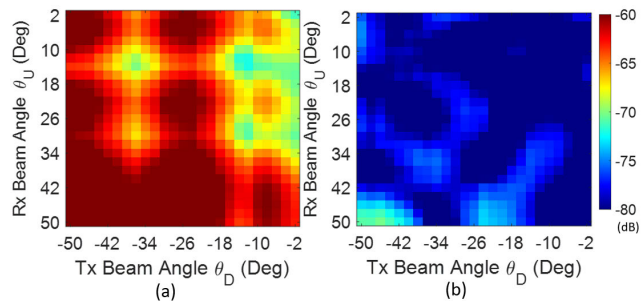
As the distance between the Tx element and the absorber increases, a decrease in isolation improvement can be observed. This reduction is attributed to the diminishing influence and contribution of near-field MC on the total SI. Furthermore, when the distance exceeds the absorber's optimal range, defined by its resonant wavelength, the interaction between the incident wave and the absorber surface becomes weaker, further diminishing its effectiveness in isolation improvement.

C. MEASURED BEAM MC WITH/WITHOUT THE ABSORBER

Antenna arrays play an essential role in enhancing spatial isolation in FD communications. Through beamforming techniques, these arrays concentrate radiation power, enabling effective management of the interactions between Tx and Rx beams. The proposed metamaterial absorber structure focuses on mitigating the near-field coupling wave components. Therefore, to evaluate the effectiveness of the metamaterial absorber structure in beam-level isolation, we first focus on the near-field dominant beam MC scenarios, where the Tx and Rx beams are steering away from each other to minimize the interaction between the far-field beams as shown in Fig. 2 (b). A study of both near-field and far-field beam-level isolation will be presented in Section V.

To evaluate the absorber improvement in the beam-level isolation, we consider the Tx-Rx beam pairs $\theta_D \in [−50° : 2° : −2°]$ and $\theta_U \in [2° : 2° : 50°]$. Therefore total of 25×25.625 pairs of Tx/Rx beam pairs are measured. The measurement results without and with the proposed metamaterial absorber structure are presented in Fig. 16.

The addition of a strategically placed absorber structure significantly reduces the MC between the Tx and Rx beams. Without the metamaterial absorber, an average beam MC of $−60.6$ dB, ranging from $−53.4$ dB to $−72.1$ dB can observed. When the absorber structure is vertically inserted between the Tx and Rx arrays, an average beam MC of $−79.2$ dB can be achieved, which indicates an average beam isolation improvement of 18.6 dB. Notably, all 625 beam pairs measured achieve isolation better than 70.3 dB with the absorber, representing a 16.9 dB improvement in the worst (highest) beam MC. The most substantial isolation improvement occurs at $(\theta_D, \theta_U) = (−48°, 38°)$ and an isolation improvement of 42.0 dB can be achieved.
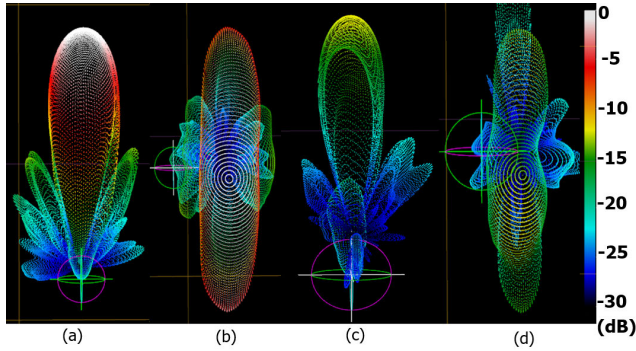
FIGURE 17. 3D beam patterns of the Tx/Rx 1 × 8 sub-arrays: (a) Tx side view, (b) Tx top view, (c) Rx side view, (d) Rx top view (measured results).

TABLE 4. Tx 1 × 8 sub-array Beam Measured Results (without absorber) (BW: Beamwidth; SLL: Sidelobe Level).

Steering angle (θ_D) (deg)	Achieved Angle(deg)	Directivity (dB)	3dB BW(deg)	10dB BW (deg)	SLL (dB)
-60	-58.1	11.6	23.4	46.1	-7.8
-50	-48.8	12.9	18.6	31.9	-7.6
-40	-41	13	17.2	29.6	-9.3
-30	-30.2	13	15.9	26.9	-10.1
-20	-21.3	13.3	16	26.7	-13
-10	-9.2	13.9	14.7	24.9	-13.2
0	0.9	14	14.2	24	-13.6
10	9.7	14	13.8	23.5	-14.1
20	20.3	13.4	15.4	26.2	-12.4
30	30.6	13.2	16.4	27.6	-14.5
40	42.3	13.1	17.8	30.9	-11.6
50	49	13.2	19.2	34	-10.6
60	59.3	11.5	22.8	41.7	-5.6

The highest (best) isolation of 104.4 dB can be achieved, which indicates a significant 32.3 dB increase compared to cases without the absorber shown in Fig. 16 (a). Out of the 625 tested beam pairs, 609 pairs (approximately 97%) exhibit an isolation improvement exceeding 10 dB, 490 pairs (around 78%) show more than 15 dB improvement, and 234 pairs (about 37%) achieve an increase in isolation beyond 20 dB. These results underscore the efficacy of the absorber structure in enhancing beam isolation across a wide range of near-field coupling dominant test cases.

D. ABSORBER IMPACTS ON THE BEAMFORMING PERFORMANCE

1) TX/RX 1 × 8 SUB-ARRAY BEAMFORMING WITHOUT THE ABSORBER

The measured normalized 3D radiation pattern of the Tx 1 × 8 and Rx 1 × 8 sub-arrays with uniform feeding power and zero phase shift at 3.5 GHz in the anechoic chamber are shown in Fig. 17. Both sub-arrays have a very similar plate-shaped beam, with two sidelobes on the two sides of the main lobe. The directivity of the Tx 1 × 8 sub-array is 14.0 dB, and the directivity of the Rx 1 × 8 sub-array is 14.9 dB. The Tx and Rx sub-arrays have 3dB-beamwidths of 14.2° and 13.4° in the Azimuth direction, respectively. The normalized side lobe level is −13.6 dB for the Tx sub-array and −13.0 dB for the Rx sub-array.

The Tx 1 × 8 sub-array is used for the experimental beam steering investigation. The beam characteristics (measured results) within the steering range −60° to 60° at

3.5 GHz are summarized in Table 4 for the case without absorber. An effective beam peak steering range from −58.1° to 59.3° is achieved. Within the steering range from −50° to 50°, an average directivity of 13.4 dB, an average 3dB-beamwidth of 16.3 degrees, and an average 10dB-beamwidth of 27.8 degrees can be achieved. Within this range, the 3dB- and 10dB-beamwidths are narrower than 19.2 and 34 degrees, respectively. The simulation and experimental results are in good agreement, with average directivity and 3dB-beamwidth difference of 0.1 dB and 0.8 degrees, respectively. The sidelobe level is lower than the main lobe by −9.3 dB in the steering range of −40° to 50°. The sidelobe increases quickly when the steering angle is larger than 50°. As the steering angle increases, the effective spacing between elements, in terms of wavelength, also increases due to the projected element spacing along the beam direction. This can result in element spacing effectively exceeding half a wavelength, leading to the formation of grating lobes, which leads to a faster sidelobe increase.

2) ABSORBER EFFECTS ON THE SUB-ARRAY FAR-FIELD PATTERN

The observed beam patterns indicate that the array possesses an effective steering range extending from −50° to +50°. Steering the sub-array beyond this angular range results in a notable expansion of the main lobe's 3dB- and 10dB-beamwidths. Such expansions lead to a rapid degradation in beam resolution. To examine the impact of the absorber on the beam radiation patterns, the Tx 1 × 8 sub-array is steered from −50° to +50° with a 10° step size. The vertically-mounted absorber is 8 cm from the Tx array. The beam-pattern azimuth-cut comparison at eight sample steering angles is shown in Fig. 18. It can be observed that the main lobes with and without the absorber overlap each other within the steering range $\theta_D \in [-50°, 40°]$. The measurement results are in line with the simulation findings. Within this range, the average difference in the directivity, the 3dB-beamwidth, the 10dB-beamwidth, and the normalized sidelobe level are 0.2 dB, 0.8 degrees, 0.9 degrees, and 0.9 dB, respectively. In other words, adding the absorber (located 8 cm away from the Tx array) has a negligible influence on the Tx 1 × 8 sub-arrays far-field beam pattern during the beamforming process. This observation also illustrates that the absorber, designed to improve near-field isolation, has limited impacts on the far-field waves.

When the steering angle $\theta_D \geq 50°$, the beam sidelobe level increases quickly. As illustrated in Fig. 18 (h), although the shape of the main lobe remains similar, the beam sidelobe level grows by 2 dB when $\theta_D \geq 50°$, due to the absorber blocking the path of the steering beam's propagation. When the blockage happens, the absorber inadvertently dissipates waves that are radiating in the target directions, which would otherwise contribute to the main lobe, thus reducing the antenna's directivity. This unintended interaction results in an elevation of the side lobes and an expansion of the main
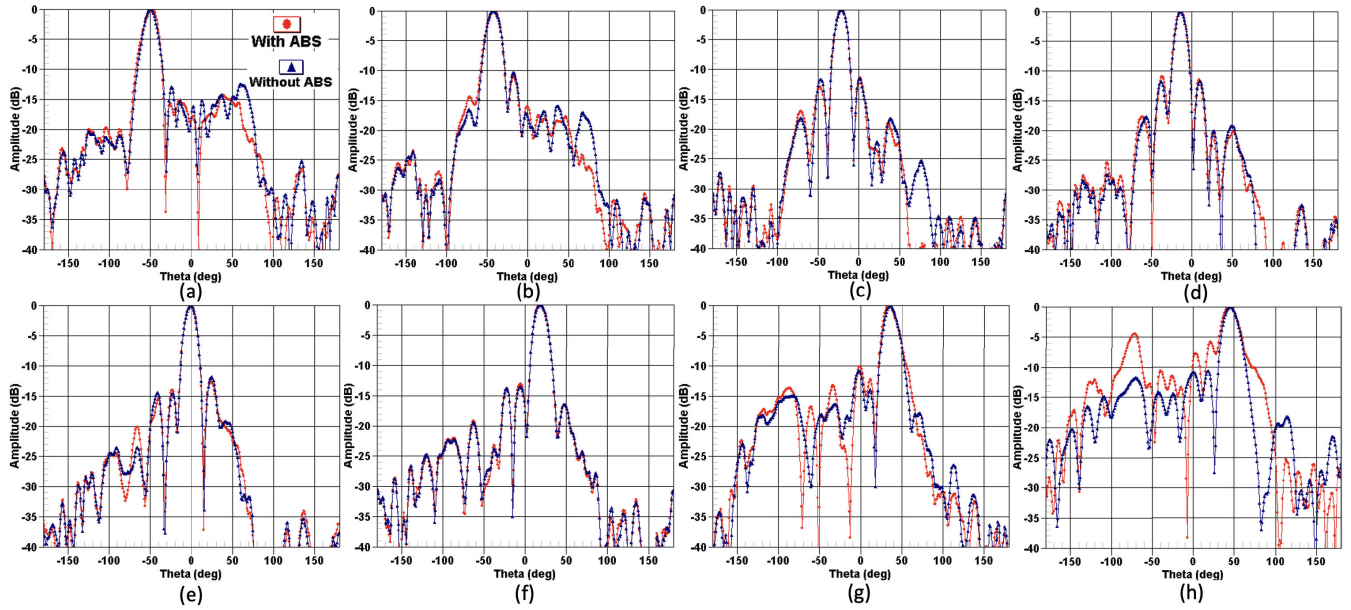
FIGURE 18. Tx 1 × 8 sub-array beams (with and without absorber) at different steering angles at (a) $\theta_D = -50°$, (b) $\theta_D = -40°$, (c) $\theta_D = -20°$, (d) $\theta_D = -10°$, (e) $\theta_D = 0°$, (f) $\theta_D = 10°$, (g) $\theta_D = 40°$, (h) $\theta_D = 50°$ (measured results).

lobe's beamwidth, causing the energy to scatter in undesired directions and reducing the array's directivity.

V. METAMATERIAL ABSORBER WITH BEAMFORMING ISOLATION OPTIMIZATION

In Section IV.C, our study focused on the efficacy of the metamaterial absorber in improving isolation, particularly in conditions where Tx-Rx far-field beam interactions are minimized. This section aims to demonstrate the performance of a combined two-stage isolation design, where using a metamaterial absorber to suppress near-field coupling, complemented by beam angle perturbations to address far-field components. The experimental findings highlight two insights:

1) The necessity of a metamaterial absorber for managing near-field MC components in guaranteeing the overall beamforming isolation design within the steering range. Otherwise, the isolation performance can be predominantly constrained by the near-field SI, especially when the beams are oriented away from each other and the Tx-Rx beam interaction is minimal.

2) Incorporating an absorber structure streamlines the beam-level optimization process. By employing the absorber structure, we can achieve a significant average isolation level of 90 dB, with a simple beam angle perturbation technique.

In Fig. 19, we present the experimental results of Tx-Rx beam isolation, encompassing four distinct scenarios:

- Scenario 1: without the absorber and beam steering angle at exact (θ_D, θ_U). This scenario serves as a baseline with no extra isolation improvement.
- Scenario 2: without the absorber, but employing beam angle perturbation for isolation optimization technique, thereby steering the beams to adjusted angles $(\hat{\theta}_D, \hat{\theta}_U)$ and targeting on far-field isolation improvement.
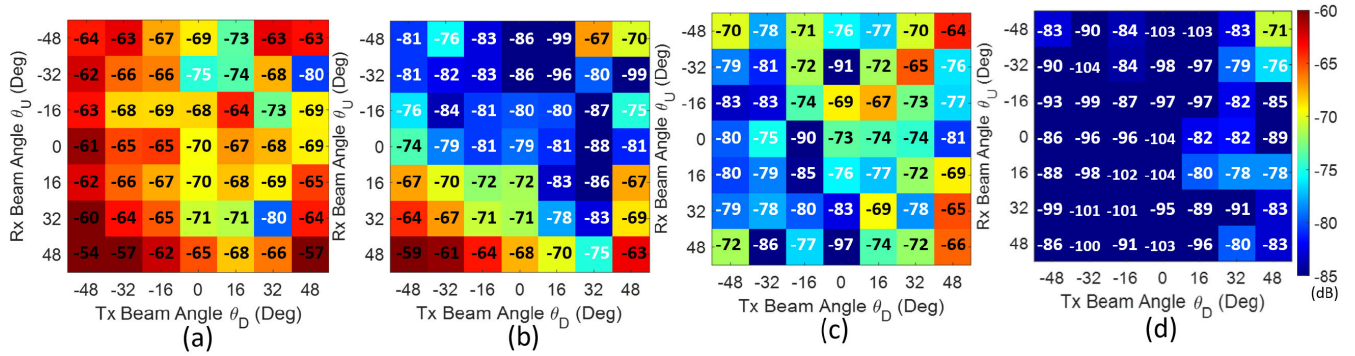
- Scenario 3: with the metamaterial absorber while steering the beams at exact (θ_D, θ_U) angles, leading to an enhancement in near-field isolation.
- Scenario 4: the combination of the metamaterial absorber with adjusted beam steering angles at $(\hat{\theta}_D, \hat{\theta}_U)$, aiming to optimize both near-field and far-field isolation.

A. ANGULAR-PERTURBATION FAR-FIELD ISOLATION IMPROVEMENT

Beamforming plays a crucial role in enhancing spatial isolation by 1) generating directional beams that confine radiation power towards the intended user, minimizing power leakage into potential interference paths; 2) focusing the Rx beams to the directions where interference radiation is nullified, reducing the receiver's detection sensitivity to interference signals.

Therefore, isolation improvement in FD mMIMO systems can be effectively achieved through beam angle perturbation techniques [36]. Rather than aligning the Tx and Rx beams precisely at the target angles θ_D and θ_U, which maximize beam directivity, we allow for a minor variation in the beam steering angles. This approach involves searching for new steering angles $(\hat{\theta}_D, \hat{\theta}_U)$ that prioritize achieving the highest possible isolation, albeit with a minor compromise in directivity. For an FD mMIMO system equipped with DL and UL RF beamformers $\mathbf{F}_D$ and $\mathbf{F}_U$, we can formulate the optimization problem for Tx-Rx isolation as follows

$$\min_{\{\hat{\theta}_D, \hat{\theta}_U\}} \left| \mathbf{F}_U(\hat{\theta}_U) \mathbf{H}_{SI} \mathbf{F}_D(\hat{\theta}_D) \right|^2$$

$$\text{s.t. } C_1 : |\hat{\theta}_D - \theta_D| \leq \epsilon_{DL},$$
$$C_2 : |\hat{\theta}_U - \theta_U| \leq \epsilon_{UL}, \qquad (7)$$

FIGURE 19. Beam MC between the sample Tx-1 × 8 and Rx-1 × 8 sub-arrays (a) without the absorber and steering at (θ_D, θ_U), (b) without the absorber and steering at $(\hat{\theta}_D, \hat{\theta}_U)$, (c) with the absorber and steering at (θ_D, θ_U), (d) with the absorber and steering at $(\hat{\theta}_D, \hat{\theta}_U)$ (measured results).

where C_1 and C_2 refer to the beam angle perturbation constraints in desired DL and UL beam directions, respectively. In our experiments, a maximum DL and UL beam angle variation within a 3dB-beamwidth range is allowed, with a center at the desired DL and UL beam angles θ_D and θ_U. The constraints indicate a maximum 3 dB directivity degradation. The proposed 1×8 sub-arrays have an average 3dB-beamwidth around 16°. Therefore, $\epsilon_{DL} = \epsilon_{UL} = 8°$. When an exhaustive search scheme is used in finding the $(\hat{\theta}_D, \hat{\theta}_U)$, the computational complexity and the number of measurement iterations increase with the resolution of the searching angle steps ($\Delta\theta$). Therefore, to mitigate the complexity involved in angle searching, our experiments adopt a large search step of 2°, i.e., $\hat{\theta}_D \in \{\theta_D - 8° : 2° : \theta_D + 8°\}$ and $\hat{\theta}_U \in \{\theta_U - 8° : 2° : \theta_U + 8°\}$.

1) EXPERIMENTAL MEASUREMENTS

In comparing beam-level MC as shown in Fig. 19 (a) and Fig. 19 (b), it can be observed that implementing beam angle perturbations for Tx/Rx can effectively lower (improve) the beam MC by 10.5 dB, reducing the average MC level from −66.5 dB to −77.0 dB. The effectiveness of this isolation enhancement, however, is notably influenced by the directional orientation of the Tx and Rx beams. For instance, when Tx and Rx beams are oriented towards each other (i.e., $\theta_D > 0°$ and $\theta_U < 0°$), an average isolation improvement of 13.9 dB, with a maximum of 25.6 dB, can be observed. The strong interaction between the Tx and Rx beams results in the high effectiveness of the approach when there is a change in the mainlobe direction.

On the other hand, as demonstrated in the lower left quadrant of Fig. 19 (b), the performance of the beamforming isolation is limited when $\theta_D < 0°$ and $\theta_U > 0°$. An average MC of −66.0 dB and the highest (worst) MC of −58.8 dB can be observed. This scenario only allows for a marginal isolation improvement of 4.2 dB through far-field beam angle perturbation. Such constraints are primarily attributed to reduced Tx/Rx beam interaction and the dominance of near-field coupling waves, due to the Tx and Rx beams' main lobes directing away from each other. Consequently,

effectively mitigating near-field SI components is essential for enhancing overall beam-level isolation in the FD systems.

B. METAMATERIAL ABSORBER NEAR-FIELD ISOLATION IMPROVEMENT

When comparing the beam-level isolation shown in Fig. 19 (a) and (c), the introduction of the metamaterial absorber structure results in a notable isolation improvement of 9.6 dB, reducing the average MC from −66.5 dB to −76.1 dB. Additionally, the orientation of the Tx and Rx beams which control the far-field beam interaction still impacts the effectiveness of this improvement. When the Tx and Rx beams are steered away from each other (i.e., $\theta_D < 0°$ and $\theta_U > 0°$), a more considerable isolation enhancement can be observed with an average isolation improvement of 17.5 dB and the maximum enhancement reaching up to 28.9 dB in the tested cases. An average beam MC of −79.4 dB can be achieved.

Furthermore, as the Tx beams are steered towards the Rx sub-array, i.e., when (θ_D, θ_U) pair moves towards the right half of Fig. 19 (c), the level of isolation improvement decreases. In beam pairs that $\theta_D > 0°$ and $\theta_U < 0°$, an average MC of −71.3 dB is observed, which is 8.1 dB higher (worse) than the case when $\theta_D < 0°$ and $\theta_U > 0°$. This reduction in isolation performance is mainly attributed to the stronger interaction between the far-field components of the Tx and Rx beams, where far-field coupling becomes increasingly dominant in the total SI.

C. COMBINED NEAR-FIELD AND FAR-FIELD ISOLATION IMPROVEMENT

From the experimental results in Fig. 19 (b) and Fig. 19 (c), following observations can be made

- The Angular-Based Beamforming Isolation Technique, primarily aimed at mitigating far-field coupling, demonstrates its effectiveness in scenarios characterized by strong interactions between the Tx and Rx beams. However, its performance tends to be limited in situations where the interaction between Tx and Rx beams is weak. In such cases, the near-field coupling component

becomes the dominant factor, thus constraining the overall isolation performance.

- The Metamaterial Absorber Technique can effectively mitigate the near-field coupling. At the same time, it is important to note that in scenarios where far-field coupling is dominant, additional isolation techniques are important to enhance the overall isolation performance.

As a result, combining these two techniques could potentially yield high isolation performance and eliminate the limitations of both methods in FD communications. The corresponding experimental results are depicted in Fig. 19 (d). Across 49 tested cases, an average Tx-Rx beam-level MC of −90.8 dB can be achieved, indicating an average improvement of 24.2 dB compared to scenarios without the absorber and beam-angle optimization. The highest recorded isolation level is 104.4 dB. All 49 beam pairs achieve a beam isolation level better than 70.8 dB.

Moreover, among the 49 Tx-Rx beam pairs, except for 5 cases, all others show an MC better (lower) than −80 dB. Notably, more than half of the tested cases (26 out of 49) achieve a beam MC lower than −90 dB. When there is no absorber and the beam angle-perturbation isolation technique, only two Tx/Rx beam pairs reach the MC level lower (better) than −80 dB, and 39 angle pairs (or 80% of the measured beam pairs) exhibit an MC worse (higher) than −70 dB, as shown in Fig. 19 (a)).

Additionally, the beam-level isolation diminishes as the θ_D becomes larger, i.e., the Tx beam steering more towards the Rx sub-array. Further far-field isolation can be achieved by either decreasing angular-perturbation step $\Delta\theta$ or implementing arbitrary beamforming nulling techniques in these beam pairs.

VI. CONCLUSION

This paper presents our design and study of a metamaterial absorber structure for FD mMIMO Tx-Rx antenna isolation improvement. The design processes of the absorber unit element, absorber placement, and influence on the beamforming radiation patterns are investigated. Working with our 8×8Tx/8×8Rx FD mMIMO antenna array prototype, an average Tx-Rx antenna element mutual coupling level of −65.4 dB is achieved between the closest Tx-Rx element pairs, which shows an improvement of 17.5 dB isolation by adding the absorber. Illustrative results using Tx/Rx 1×8 sub-arrays indicate an average 18.6 dB isolation improvement in near-field dominant SI scenarios. Experimental investigations on the correlation between the near-field and far-field dominant SI scenarios and the downlink and uplink beam directions are conducted. The critical role of the absorber structure in managing near-field self-interference, thereby ensuring the efficacy of the overall beamforming isolation performance, is demonstrated. Combined with a simple angular perturbation beam isolation technique, an average Tx-Rx beam-level isolation of 90.8 dB with a maximum beam isolation level of 104.4 dB can be achieved within a

Tx/Rx steering range −48° to 48° with 20 MHz modulated signals.

REFERENCES

[1] A. Sabharwal, P. Schniter, D. Guo, D. W. Bliss, S. Rangarajan, and R. Wichman, "In-band full-duplex wireless: Challenges and opportunities," *IEEE J. Sel. Areas Commun.*, vol. 32, no. 9, pp. 1637–1652, Sep. 2014.

[2] Z. Zhang, X. Chai, K. Long, A. V. Vasilakos, and L. Hanzo, "Full duplex techniques for 5G networks: Self-interference cancellation, protocol design, and relay selection," *IEEE Commun. Mag.*, vol. 53, no. 5, pp. 128–137, May 2015.

[3] B. Smida, A. Sabharwal, G. Fodor, G. C. Alexandropoulos, H. A. Suraweera, and C.-B. Chae, "Full-duplex wireless for 6G: Progress brings new opportunities and challenges," *IEEE J. Sel. Areas Commun.*, vol. 41, no. 9, pp. 2729–2750, Sep. 2023.

[4] M. Duarte, C. Dick, and A. Sabharwal, "Experiment-driven characterization of full-duplex wireless systems," *IEEE Trans. Wireless Commun.*, vol. 11, no. 12, pp. 4296–4307, Dec. 2012.

[5] B. Debaillie, D.-J. van den Broek, C. Lavín, B. van Liempd, E. A. M. Klumperink, C. Palacios, J. Craninckx, B. Nauta, and A. Pärssinen, "Analog/RF solutions enabling compact full-duplex radios," *IEEE J. Sel. Areas Commun.*, vol. 32, no. 9, pp. 1662–1673, Sep. 2014.

[6] M. Chung, M. S. Sim, J. Kim, D. K. Kim, and C.-B. Chae, "Prototyping real-time full duplex radios," *IEEE Commun. Mag.*, vol. 53, no. 9, pp. 56–63, Sep. 2015.

[7] M. Duarte, A. Sabharwal, V. Aggarwal, R. Jana, K. K. Ramakrishnan, C. W. Rice, and N. K. Shankaranarayanan, "Design and characterization of a full-duplex multiantenna system for WiFi networks," *IEEE Trans. Veh. Technol.*, vol. 63, no. 3, pp. 1160–1177, Mar. 2014.

[8] W. T. Slingsby, "Antenna isolation measurements for on-frequency radio repeaters," in *Proc. 9th Int. Conf. Antennas Propag. (ICAP)*, Apr. 1995, pp. 239–243.

[9] E. Everett, A. Sahai, and A. Sabharwal, "Passive self-interference suppression for full-duplex infrastructure nodes," *IEEE Trans. Wireless Commun.*, vol. 13, no. 2, pp. 680–694, Feb. 2014.

[10] H. Nawaz and I. Tekin, "Dual-polarized, differential fed microstrip patch antennas with very high interport isolation for full-duplex communication," *IEEE Trans. Antennas Propag.*, vol. 65, no. 12, pp. 7355–7360, Dec. 2017.

[11] C.-Y.-D. Sim, C.-C. Chang, and J.-S. Row, "Dual-feed dual-polarized patch antenna with low cross polarization and high isolation," *IEEE Trans. Antennas Propag.*, vol. 57, no. 10, pp. 3405–3409, Oct. 2009.

[12] A. Ramos, T. Varum, and J. N. Matos, "A review on mutual coupling reduction techniques in mmWaves structures and massive MIMO arrays," *IEEE Access*, vol. 11, pp. 143143–143166, 2023.

[13] M. Yang, C. Liu, and X. Liu, "Design of π-shaped decoupling network for dual-polarized Y-probe antenna arrays," *IEEE Antennas Wireless Propag. Lett.*, vol. 21, pp. 1129–1133, 2022.

[14] D. Wu, S. W. Cheung, Q. L. Li, and T. I. Yuk, "Decoupling using diamond-shaped patterned ground resonator for small MIMO antennas," *IET Microw., Antennas Propag.*, vol. 11, no. 2, pp. 177–183, Jan. 2017.

[15] I. A. Tunio, Y. Mahe, T. Razban-Haghighi, and B. Froppier, "Mutual coupling reduction in patch antenna array using combination of shorting pins and metallic walls," *Prog. Electromagn. Res. C*, vol. 107, pp. 157–171, 2021.

[16] K. Iwamoto, M. Heino, K. Haneda, and H. Morikawa, "Design of an antenna decoupling structure for an inband full-duplex collinear dipole array," *IEEE Trans. Antennas Propag.*, vol. 66, no. 7, pp. 3763–3768, Jul. 2018.

[17] M. Abedian, M. Khalily, P. Xiao, F. Wang, R. Tafazolli, and A. A. Kishk, "MM-wave high isolated dual polarized dielectric resonator antenna for in-band full-duplex systems," *IEEE Access*, vol. 11, pp. 38218–38225, 2023.

[18] R. Askar and W. Keusgen, "Lossless decoupling networks for RF self-interference cancellation in MIMO full-duplex transceivers," *IEEE J. Sel. Areas Commun.*, vol. 41, no. 9, pp. 2765–2779, Sep. 2023.

[19] J. Wu, M. Li, and N. Behdad, "A wideband, unidirectional circularly polarized antenna for full-duplex applications," *IEEE Trans. Antennas Propag.*, vol. 66, no. 3, pp. 1559–1563, Mar. 2018.

[20] D. Wu, Y.-X. Sun, B. Wang, and R. Lian, "A compact, monostatic, co-circularly polarized simultaneous transmit and receive (STAR) antenna with high isolation," *IEEE Antennas Wireless Propag. Lett.*, vol. 19, pp. 1127–1131, 2020.

[21] D. Ahn, J.-S. Park, C.-S. Kim, J. Kim, Y. Qian, and T. Itoh, "A design of the low-pass filter using the novel microstrip defected ground structure," *IEEE Trans. Microw. Theory Techn.*, vol. 49, no. 1, pp. 86–93, Jan. 2001.

[22] A. Madni and W. Tanveer Khan, "Design of a compact 4-element GNSS antenna array with high isolation using a defected ground structure (DGS) and a microwave absorber," *IEEE Open J. Antennas Propag.*, vol. 4, pp. 779–791, 2023.

[23] S. Ghosh, T.-N. Tran, and T. Le-Ngoc, "Dual-layer EBG-based miniaturized multi-element antenna for MIMO systems," *IEEE Trans. Antennas Propag.*, vol. 62, no. 8, pp. 3985–3997, Aug. 2014.

[24] H. S. Farahani, M. Veysi, M. Kamyab, and A. Tadjalli, "Mutual coupling reduction in patch antenna arrays using a UC-EBG superstrate," *IEEE Antennas Wireless Propag. Lett.*, vol. 9, pp. 57–59, 2010.

[25] N. I. Landy, S. Sajuyigbe, J. J. Mock, D. R. Smith, and W. J. Padilla, "Perfect metamaterial absorber," *Phys. Rev. Lett.*, vol. 100, no. 20, May 2008, Art. no. 207402.

[26] F. Tofigh, M. Amiri, N. Shariati, J. Lipman, and M. Abolhasan, "Polarization-insensitive metamaterial absorber for crowd estimation based on electromagnetic energy measurements," *IEEE Trans. Antennas Propag.*, vol. 68, no. 3, pp. 1458–1467, Mar. 2020.

[27] A. Jafargholi, A. Jafargholi, and J. H. Choi, "Mutual coupling reduction in an array of patch antennas using CLL metamaterial superstrate for MIMO applications," *IEEE Trans. Antennas Propag.*, vol. 67, no. 1, pp. 179–189, Jan. 2019.

[28] J. Zhang, J. Li, and J. Chen, "Mutual coupling reduction of a circularly polarized four-element antenna array using metamaterial absorber for unmanned vehicles," *IEEE Access*, vol. 7, pp. 57469–57475, 2019.

[29] G. Zhai, Z. N. Chen, and X. Qing, "Enhanced isolation of a closely spaced four-element MIMO antenna system using metamaterial mushroom," *IEEE Trans. Antennas Propag.*, vol. 63, no. 8, pp. 3362–3370, Aug. 2015.

[30] W. J. Padilla and K. Fan, "Metamaterial electromagnetic wave absorbers," *Synth. Lectures Electromagn.*, vol. 3, no. 1, pp. 1–199, Jan. 2022.

[31] Z. Qamar, U. Naeem, S. A. Khan, M. Chongcheawchamnan, and M. F. Shafique, "Mutual coupling reduction for high-performance densely packed patch antenna arrays on finite substrate," *IEEE Trans. Antennas Propag.*, vol. 64, no. 5, pp. 1653–1660, May 2016.

[32] Q.-L. Zhang, Y.-T. Jin, J.-Q. Feng, X. Lv, and L.-M. Si, "Mutual coupling reduction of microstrip antenna array using metamaterial absorber," in *IEEE MTT-S Int. Microw. Symp. Dig.*, Jul. 2015, pp. 1–3.

[33] M. Agarwal and M. K. Meshram, "Isolation improvement of 5 GHz WLAN antenna array using metamaterial absorber," in *Proc. URSI Asia–Pacific Radio Sci. Conf. (URSI AP-RASC)*, Aug. 2016, pp. 1050–1053.

[34] C. Wang, X. Yang, and B. Wang, "A metamaterial-based compact broadband planar monopole MIMO antenna with high isolation," *Microw. Opt. Technol. Lett.*, vol. 62, no. 9, pp. 2965–2970, May 2020.

[35] D. H. Truyen Hoang, V. X. Trung Nguyen, T. T. Do, D. N. Nguyen, T. A. Vu, and Q. N. Tran, "Mutual coupling reduction of MIMO antenna using metamaterial absorber for 5G base stations," in *Proc. Asia–Pacific Microw. Conf. (APMC)*, Nov. 2022, pp. 767–769.

[36] Y. Gong, M. Mahmood, R. Morawski, and T. Le-Ngoc, "Dual-layer metamaterial rectangular antenna arrays for in-band full-duplex massive MIMO," *IEEE Access*, vol. 11, pp. 135708–135727, 2023.

[37] A. Koc and T. Le-Ngoc, "Full-duplex mmWave massive MIMO systems: A joint hybrid precoding/combining and self-interference cancellation design," *IEEE Open J. Commun. Soc.*, vol. 2, pp. 754–774, 2021.

[38] A. Koc and T. Le-Ngoc, "Intelligent non-orthogonal beamforming with large self-interference cancellation capability for full-duplex multiuser massive MIMO systems," *IEEE Access*, vol. 10, pp. 51771–51791, 2022.

[39] Z. Luo, L. Zhao, L. Tonghui, H. Liu, and R. Zhang, "Robust hybrid precoding/combining designs for full-duplex millimeter wave relay systems," *IEEE Trans. Veh. Technol.*, vol. 70, no. 9, pp. 9577–9582, Sep. 2021.

[40] N. Fatema, G. Hua, Y. Xiang, D. Peng, and I. Natgunanathan, "Massive MIMO linear precoding: A survey," *IEEE Syst. J.*, vol. 12, no. 4, pp. 3920–3931, Dec. 2018.

[41] Y. Gong, A. Yaseen, R. Morawski, and T. Le-Ngoc, "Perturbation-based adaptive beamforming for MU-mMIMO," in *Proc. IEEE 98th Veh. Technol. Conf. (VTC-Fall)*, Oct. 2023, pp. 1–5.

[42] Y. Gong, R. Morawski, H. H. Lee, and T. Le-Ngoc, "A miniaturized 8×8 dual-layer EBG slotted circularly polarized patch antenna array for mMIMO," in *Proc. IEEE Global Commun. Conf. (GLOBECOM)*, Dec. 2022, pp. 6511–6516.

YUANZHE GONG (Graduate Student Member, IEEE) received the B.Sc. degree (Hons.) in electrical and computer engineering from McGill University, Montreal, Canada, in 2020, where he is currently pursuing the Ph.D. degree in electrical engineering. Since 2018, he has been a Teaching Assistant with the Electrical and Computer Engineering Department, McGill University. His research interests include wireless communications, antenna design, metamaterial absorbers, massive MIMO, and full-duplex. He was a recipient of the McGill Engineering Doctoral Award by McGill University.

ROBERT MORAWSKI received the B.Sc. and M.Sc. degrees in electrical and computer engineering from Concordia University, Montreal, Canada, in 1997 and 2000, respectively. He is currently a Research Engineer and the Laboratory Manager with the Broadband Communications Research Laboratory, ECE Department, McGill University, Montreal. His research interest includes the design and implementation of prototype architectures for next-generation wireless communications.

THO LE-NGOC (Life Fellow, IEEE) received the B.Eng. degree in electrical engineering, in 1976, the M.Eng. degree in microprocessor applications from McGill University, Montreal, in 1978, and the Ph.D. degree in digital communications from the University of Ottawa, Canada, in 1983.

From 1977 to 1982, he was with SparAerospace Ltd., Sainte-Anne-de-Bellevue, QC, Canada, involved in the development and design of satellite communications systems. From 1982 to 1985, he was with SRTelecom Inc., Saint-Laurent, QC, where he developed the new point-to-multipoint DA-TDMA/TDM Subscriber Radio System SR500. From 1985 to 2000, he was a Professor with the Department of Electrical and Computer Engineering, Concordia University, Montreal. Since 2000, he has been with the Department of Electrical and Computer Engineering, McGill University. His research interest includes broadband digital communications.

Dr. Le-Ngoc is a fellow of the Engineering Institute of Canada, the Canadian Academy of Engineering, and the Royal Society of Canada. He was a recipient of the 2004 Canadian Award in Telecommunications Research and the IEEE Canada Fessenden Award, in 2005. He is a Distinguished James McGill Professor.